



A Vimentin-Targeting Oral Compound with Host-Directed Antiviral and Anti-Inflammatory Actions Addresses Multiple Features of COVID-19 and Related Diseases

Zhizhen Li,^a Jianping Wu,^{b,c} Ji Zhou,^d Baoshi Yuan,^a Jiqiao Chen,^e Wanchen Wu,^f Lian Mo,^g Zhipeng Qu,^{g*} Fei Zhou,^a Yingying Dong,^a Kai Huang,^a Zhiwei Liu,^a Tao Wang,^a Deebie Symmes,^g Jingliang Gu,^f Eiketsu Sho,^e Jingping Zhang,^d Ruihuan Chen,^{c,g} Ying Xu^a

^aJiangsu Key Laboratory of Neuropsychiatric Diseases and Cambridge-Su Genomic Resource Center, Medical School of Soochow University, Suzhou, Jiangsu, China

^bLaboratory Animal Center, Nanjing University of Chinese Medicine, Nanjing, Jiangsu, China

^cLuoda Biosciences, Inc., Chuzhou, Anhui, China

^dInstitute of Biology and Medical Sciences, Medical School of Soochow University, Suzhou, Jiangsu, China

^eKCI Biotech (Suzhou) Inc., Suzhou, Jiangsu, China

^fJoinn Laboratories (Suzhou) Co., Ltd., Suzhou, Jiangsu, China

^gAluda Pharmaceuticals, Inc., Menlo Park, California, USA

Zhizhen Li, Jianping Wu, Ji Zhou, and Baoshi Yuan contributed equally to this work. Author order was determined on the basis of affiliation.

ABSTRACT Damage in COVID-19 results from both the SARS-CoV-2 virus and its triggered overactive host immune responses. Therapeutic agents that focus solely on reducing viral load or hyperinflammation fail to provide satisfying outcomes in all cases. Although viral and cellular factors have been extensively profiled to identify potential anti-COVID-19 targets, new drugs with significant efficacy remain to be developed. Here, we report the potent preclinical efficacy of ALD-R491, a vimentin-targeting small molecule compound, in treating COVID-19 through its host-directed antiviral and anti-inflammatory actions. We found that by altering the physical properties of vimentin filaments, ALD-491 affected general cellular processes as well as specific cellular functions relevant to SARS-CoV-2 infection. Specifically, ALD-R491 reduced endocytosis, endosomal trafficking, and exosomal release, thus impeding the entry and egress of the virus; increased the microcidal capacity of macrophages, thus facilitating the pathogen clearance; and enhanced the activity of regulatory T cells, therefore suppressing the overactive immune responses. In cultured cells, ALD-R491 potently inhibited the SARS-CoV-2 spike protein and human ACE2-mediated pseudoviral infection. In aged mice with ongoing, productive SARS-CoV-2 infection, ALD-R491 reduced disease symptoms as well as lung damage. In rats, ALD-R491 also reduced bleomycin-induced lung injury and fibrosis. Our results indicate a unique mechanism and significant therapeutic potential for ALD-R491 against COVID-19. We anticipate that ALD-R491, an oral, fast-acting, and non-cytotoxic agent targeting the cellular protein with multipart actions, will be convenient, safe, and broadly effective, regardless of viral mutations, for patients with early- or late-stage disease, post-COVID-19 complications, and other related diseases.

IMPORTANCE With the Delta variant currently fueling a resurgence of new infections in the fully vaccinated population, developing an effective therapeutic drug is especially critical and urgent in fighting COVID-19. In contrast to the many efforts to repurpose existing drugs or address only one aspect of COVID-19, we are developing a novel agent with first-in-class mechanisms of action that address both the viral infection and the overactive immune system in the pathogenesis of the disease. Unlike virus-directed therapeutics that may lose efficacy due to viral mutations, and immunosuppressants that require ideal timing to be effective, this agent, with its unique host-directed antiviral and anti-inflammatory actions, can work against all

Citation Li Z, Wu J, Zhou J, Yuan B, Chen J, Wu W, Mo L, Qu Z, Zhou F, Dong Y, Huang K, Liu Z, Wang T, Symmes D, Gu J, Sho E, Zhang J, Chen R, Xu Y. 2021. A vimentin-targeting oral compound with host-directed antiviral and anti-inflammatory actions addresses multiple features of COVID-19 and related diseases. *mBio* 12:e02542-21. <https://doi.org/10.1128/mBio.02542-21>.

Editor Steven J. Projan

Copyright © 2021 Li et al. This is an open-access article distributed under the terms of the [Creative Commons Attribution 4.0 International license](#).

Address correspondence to Ruihuan Chen, ruihuan@aludapharm.com, or Ying Xu, yingxu@suda.edu.cn.

* Present address: Zhipeng Qu, Vazyme Biotech Co. Ltd., Nanjing, Jiangsu, China.

Received 25 August 2021

Accepted 1 September 2021

Published 12 October 2021

variants of the virus, be effective during all stages of the disease, and even resolve post-disease damage and complications. Further development of the compound will provide an important tool in the fight against COVID-19 and its complications, as well as future outbreaks of new viruses.

KEYWORDS COVID-19, small molecule, vimentin, host-directed antiviral, anti-inflammation

Vaccines against SARS-CoV-2 have been rapidly developed and rolled out to contain the COVID-19 pandemic; however, the infection-blocking immunity induced by vaccination has been shown to wane quickly, even though disease-reducing immunity may be long-lived (1). Vaccination primarily generates IgG antibodies that circulate in the blood, not IgA antibodies in the mucosa of the respiratory tract, which are a critical component of the mucosal immunity that prevents SARS-CoV-2 from initiating its infection (2, 3). The spike mRNA-based vaccination induces strong, persistent antibody responses but is accompanied by a limited or absent T-cell response (4, 5). In addition, the virus has now demonstrated an ability to rapidly mutate during its transmission and to generate mutants that provide not only enhanced infectivity, but also an acquired ability to escape from therapeutic antibodies and those induced by infection or vaccination. Several variants of concern (VOCs) have emerged within a short period of time, especially the Delta variant (6, 7), which is currently fueling a resurgence of new infection in fully vaccinated populations. This virus appears to present a persistent problem despite vaccines, and therefore effective therapeutics are critically needed.

To date, most therapeutic interventions have been focused on either stopping viral infection or reducing virus-induced hyperinflammation. Antiviral approaches can be virus-directed or host-directed. Virus-directed approaches include blocking viral entry, preventing maturation of viral proteins, and disrupting the viral RNA-synthesis machinery. All face challenges from the rapid viral mutations that could make them ineffective over time. In addition, these types of agents must be given early during an infection to be effective, as viral load has been shown to peak on or before symptom onset (8) with very few infectious viruses present in the upper respiratory tract 10 days after the onset of symptoms, even without treatment (9). A delayed or longer antiviral treatment in the course of COVID-19 has been shown to lead to a worse outcome (10), because it is the overactivated host immune system, not the virus itself, that is driving the progression and the development of serious complications. However, immunomodulators have shown minimal effects, and corticosteroids, moderate effects only if given at the right timing, and otherwise worsening the disease. Host-directed antiviral approaches have attracted attention because targeting host proteins offers broad-spectrum antiviral actions that are hard for virus to evade through mutation. The host proteins that interact with SARS-CoV-2 have been extensively profiled, and a large quantity of existing compounds have been screened for potential antiviral activities (11–15). So far, however, no repurposed antiviral drugs addressing these host factors have shown significant efficacy in clinical trials (16).

An ideal anti-COVID-19 agent would be able to both eliminate the virus and restore balance to the immune system. Several existing drugs, such as hydroxychloroquine, colchicine, and ivermectin, that exhibit some degree of synergistic antiviral and anti-inflammatory actions, have been repurposed to treat COVID-19; however, the results have been controversial or inconclusive. Whether applied in early disease to prevent progression or in the late stage to reduce morbidity and mortality, therapeutics with new mechanisms are urgently needed to tackle the multifaceted and interrelated nature of pathogenesis in SARS-CoV-2 infection.

Vimentin, an evolutionarily very conserved intermediate filament protein with diverse functions in health and disease (17), has been proposed as a host-directed therapeutic target for COVID-19 (18, 19). Vimentin facilitates viral infection by serving as a co-receptor and as a component of the cellular transportation machinery for viral

entry, trafficking, and egress (20). Vimentin is also specifically involved in inflammatory responses, where it forms a superstructure inside regulatory T cells that mechanically regulates the switch of the cell between active and inactive status (21), and provides a scaffold structure that enables the NLRP3 inflammasome to assemble, activate, and contribute to inflammation and lung injury (22). Targeting vimentin is unlikely to generate mechanism-based toxicities because the protein has been widely recognized to be non-essential from embryonic development to adulthood ever since the first work in early 1990s demonstrated that mice lacking vimentin developed and reproduced without an obvious phenotype (23).

We synthesized a series of small molecule compounds that can bind to vimentin (24). The lead compound, ALD-R491, has shown many favorable safety features; it is fast-acting and fully reversible, has no cytotoxicity, and causes no change in the protein levels of vimentin and other proteins of major signaling pathways (25). In this study, we explored the effects of ALD-R491 on vimentin structure and function, general cellular processes, and specific cellular functions relevant to SARS-CoV-2 infection and evaluated the compound *in vitro* and *in vivo* for its antiviral and anti-inflammatory effects. The constellation of effects we observed strongly supports this oral small molecule compound as a promising host-directed therapeutic agent with novel mechanisms to address multiple pathological processes of COVID-19.

RESULTS

ALD-R491 reduces the dynamism of vimentin filaments and inhibits endocytosis, endosomal trafficking, and exosomal release. To understand the impact of the compound-binding on the target protein, we first examined the distribution of vimentin intermediate filaments (IF) in live cells. Confocal immunofluorescence imaging showed a dynamic reorganization of intracellular vimentin network responding to ALD-R491 treatment. In the control cells, the vimentin IF formed bundle-like structures parallel to the longitudinal axis of the cell, with a richer presence in the cell peripheral region and at the far end of cell than in the central region. In ALD-R491-treated cells, the vimentin IF retracted from the periphery with no structural changes visible at low doses but with an intricate, honeycomb-like reticulated structure formed in the perinuclear region at high doses (Fig. 1A). This alteration was specific to vimentin, because the proteins of the same type-III IF family, GFAP and desmin, showed no structural changes to ALD-R491 treatment. (Fig. S1A).

We next sought to determine how the altered organization of vimentin IF would relate to a change in the physical properties of ALD-R491-bound vimentin filament. We utilized the fluorescence recovery after photobleaching (FRAP) technique to quantify the two-dimensional lateral diffusion of vimentin-green fluorescent protein (GFP) in the cells treated with the compound or the solvent control. We found that the time required for fluorescence recovery in the photobleached region was significantly longer in the ALD-R491-treated cells (Fig. 1B and C), indicating that the ALD-R491-bound vimentin protein had become less mobile or had a compromised dynamism.

Vimentin is involved in the trafficking of membrane and intracellular vesicles, so we hypothesized that a decrease in mobility or dynamism would impact subcellular processes related to material transportation. To test this, we used a liposome-mediated plasmid transfection method. To separate the effect on endocytosis from that on endosomal trafficking, we treated the cells with ALD-R491 during three different time periods (Fig. 1D and E). When present during the entire transfection process (full-time) that impacts both endocytosis and trafficking, ALD-R491 reduced the levels of GFP reporter up to 50%, with a 50% effective concentration (EC_{50}) of $0.036\ \mu M$ and an EC_{90} of $0.19\ \mu M$. At $0.3\ \mu M$ ALD-R491 reached its maximum effect of 50% inhibition (treated full-time), and the inhibition rates of ALD-R491 on endocytosis (treated before transfection) and endosomal trafficking (treated after transfection) were 18% and 35%, respectively (Fig. 1E). These results indicate that endocytosis and endosomal trafficking were very sensitive to ALD-R491; however, neither of the cellular

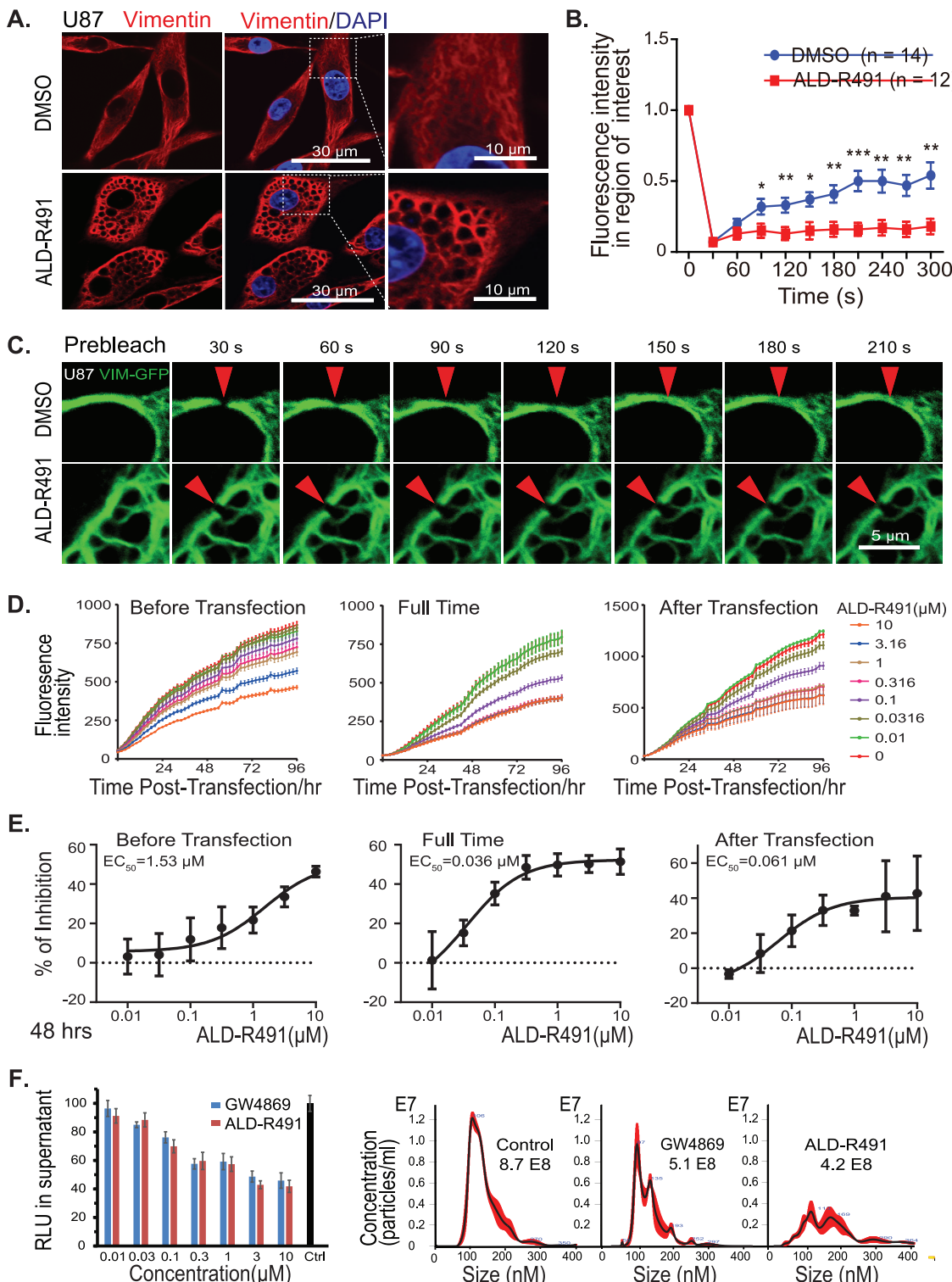


FIG 1 Effects of ALD-R491 on vimentin filaments and subcellular processes. Changes in intracellular organization and physical property of vimentin filament and reductions in endocytosis, endosomal trafficking, and exosomal release. (A) ALD-R491 induced the reorganization of vimentin intermediate filament network. (B and C) ALD-R491 compromised the mobility of vimentin filaments; (B) quantitative measurement and (C) image presentation. Two-tailed t test. *, P < 0.05; **, P < 0.01; ***, P < 0.001. (D and E) Dose-responsive inhibition on endocytosis and endosomal trafficking; (D) Fluorescence intensity over time and (E) dose-responsive reduction in GFP levels. (F) Exosome release blockade. (Left bar graph) The luciferase activity in the culture supernatant was quantified; (right) the purified exosomes were quantified by nanoparticle tracking analysis.

processes was completely blocked by the compound, with endosomal trafficking impacted more than endocytosis.

Exosomes originate from the endocytic pathway and are released via the fusion of a multivesicular body (MVB) with cell membrane (26). Using a reporter system as well as a classic exosome purification method, we found that ALD-R491 inhibited exosome release from Huh7 cells in a dose-dependent manner (Fig. 1F). Like the effects observed on endocytosis and endosomal trafficking, the maximal rates of inhibition on exosome release plateaued at around 50% of nondrug levels. These data indicate that by altering the mechanical properties ("dynamism") of vimentin filaments, ALD-R491 reduced multiple cellular processes that are related to viral entry, trafficking, and egress.

ALD-R491 blocks SARS-CoV-2 spike protein-ACE2-mediated pseudoviral infection.

Targeting the initial steps of infection, such as viral entry and decoating, is an attractive antiviral approach, particularly for a host-directed antiviral mechanism with the objective of blocking virus-host cell interactions. SARS-CoV-2 gains access into cells through endocytosis after the engagement of its spike protein with cell membrane proteins. Angiotensin-converting enzyme 2 (ACE2) is the receptor for the spike protein and is responsible for the initiation of infection, although other host factors, such as TMPRSS-2 and neuropilin-1, may facilitate the viral entry process. We tested the antiviral activity of ALD-R491 by using a lentivirus pseudotyped with the human SARS-CoV-2 spike protein to infect HEK293 cells overexpressing human ACE2 protein. Because the pseudovirus expresses both GFP and luciferase, the infection efficiency can be continuously tracked by live imaging of fluorescence and quantified at the endpoint by measuring luciferase activity. Exposure of the cells to ALD-R491 resulted in a dramatic reduction in the pseudoviral infection at all dose levels during the whole infection process (Fig. 2A and B, Fig. S2A and B) and generated no cytotoxicity even at the highest concentration tested (50% cytotoxic concentration [CC_{50}], $>10 \mu\text{M}$) (Fig. 2C). We conclude, therefore, that this antiviral effect was largely due to a blockade of viral entry rather than subsequent steps after endocytosis because no antiviral activity was observed when the compound was given 2 h after the viral infection. Regardless of the level of viral load present, ALD-R491 strongly and dose-dependently inhibited pseudoviral infection, with IC_{50} s of 13.5, 34.7, and 64.9 nM for the infections at multiplicities of infection (MOI) of 0.5, 5, and 50, respectively (Fig. 2D and E). Clearly, ALD-R491 was highly selective (>154 at an MOI of 50) and potent at blocking the spike protein-ACE2-mediated viral entry, the first step of SARS-CoV-2 infection. Unlike virus-directed approaches aimed at blocking the binding of the spike protein with ACE2 receptor, which include anti-spike protein antibodies that may become futile as the epitope of spike protein continues to mutate, our host-directed approach blocks the cellular process that is used by the virus. As long as endocytosis remains the route for their cellular entry, the compound would be equally effective for all variants.

ALD-R491 enhances macrophage's pathogen-killing efficiency. Monocytes and macrophages are the most important innate immune cells in the host defense against infections from pathogens, including viruses, fungi, and bacteria. At the early stages of an infection, the innate immune system, in particular macrophage M1, is the first line of defense that prevents pathogens that have entered the tissues from further dissemination. In addition to triggering an immune response and producing proinflammatory cytokines, macrophages effectively phagocytose these pathogens, directly destroying them inside the phagosome or lysosome. SARS-CoV-2 can interrupt phagolysosome function and even hijack the phagolysosome to egress from infected cells (27). The SARS-CoV-2 virus has been found alive inside monocytes and macrophages (28, 29), suggesting an impaired function of these cells for pathogen clearance and a problematic reservoir site that supports lingering infection. The key actor for macrophage microbicidal activity is NADPH oxidase in the phagosomes, which produces reactive oxygen species (ROS). NADPH oxidase is a membrane-associated enzyme consisting of multiple subunits. Vimentin is known to bind with p47Phox, a subunit of NADPH oxidase. The association with vimentin makes the p47phox subunit separate from the enzyme complex of NADPH oxidase, restraining the enzyme activity and thereby

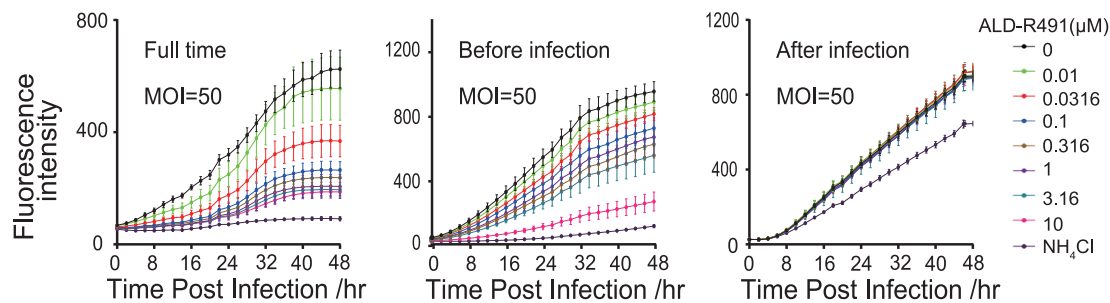
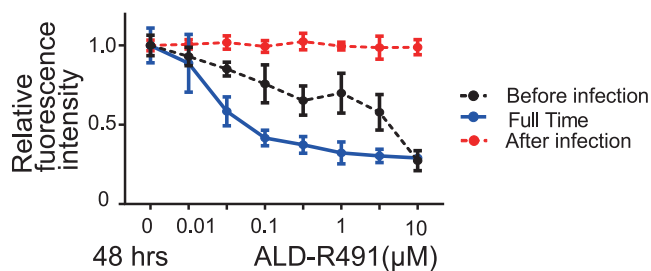
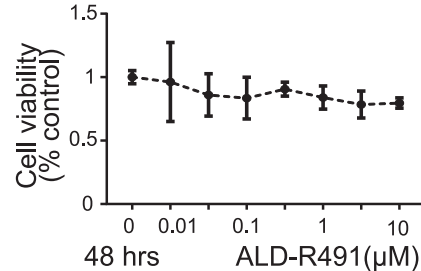
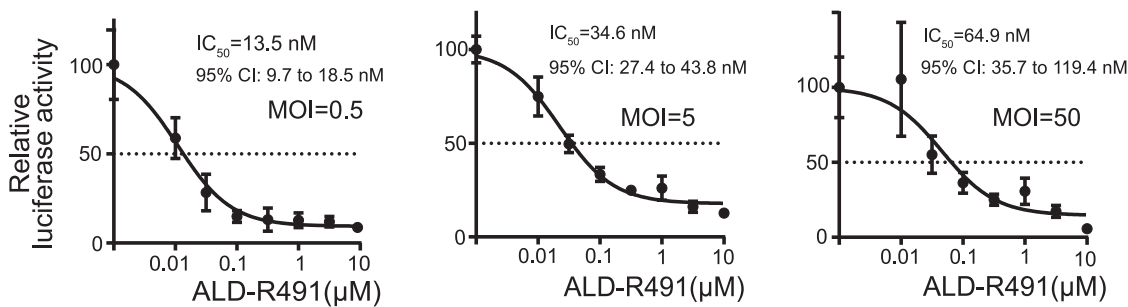
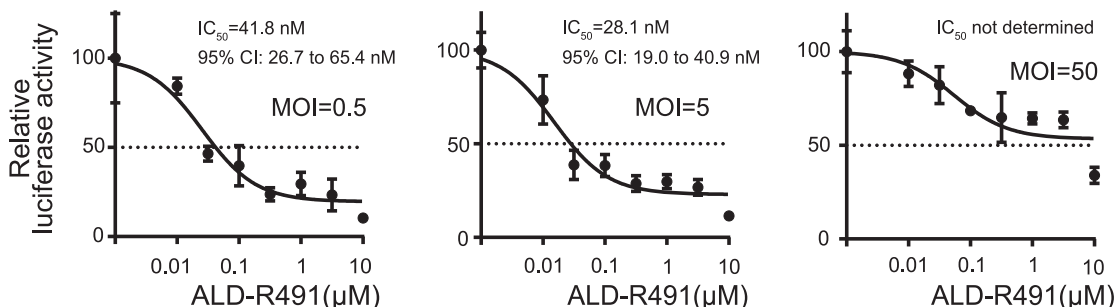
A. Time course of viral gene expression**B. Dose-responsive inhibition****C. No cytotoxic effect****D. Treatment for the full time of infection****E. Treatment before infection**

FIG 2 ALD-R491 blocked Spike protein-ACE2-mediated viral entry *in vitro*. (A) Fluorescence intensity of the GFP reporter gene expression. The HEK cells were infected by the GFP-expressing lentiviral-based pseudovirus and measured for fluorescence intensity every 2 h over the course of the experiment. The cells were treated with ALD-R491 from 2 h before the infection until the end of the experiment (left, full-time), for only 2 h before the infection with the removal of the compound upon the infection (center, before infection), and from 2 h after the infection until the end of the experiment (right, after infection). (B) Dose-dependent GFP levels at 48 h after infection. (C) No cytotoxicity associated with ALD-R491. (D and E) At the end of the experiment, luciferase activities were measured from the cell lysates. The figures show the inhibition rates of ALD-R491 at different concentrations on the infection by the pseudovirus at multiplicities of infection (MOI) of 0.5, 5, and 50, respectively. Exposure of cells to ALD-R491: (D) full-time; (E) before infection. The IC₅₀ and its 95% confidence interval (CI) are shown in the figures.

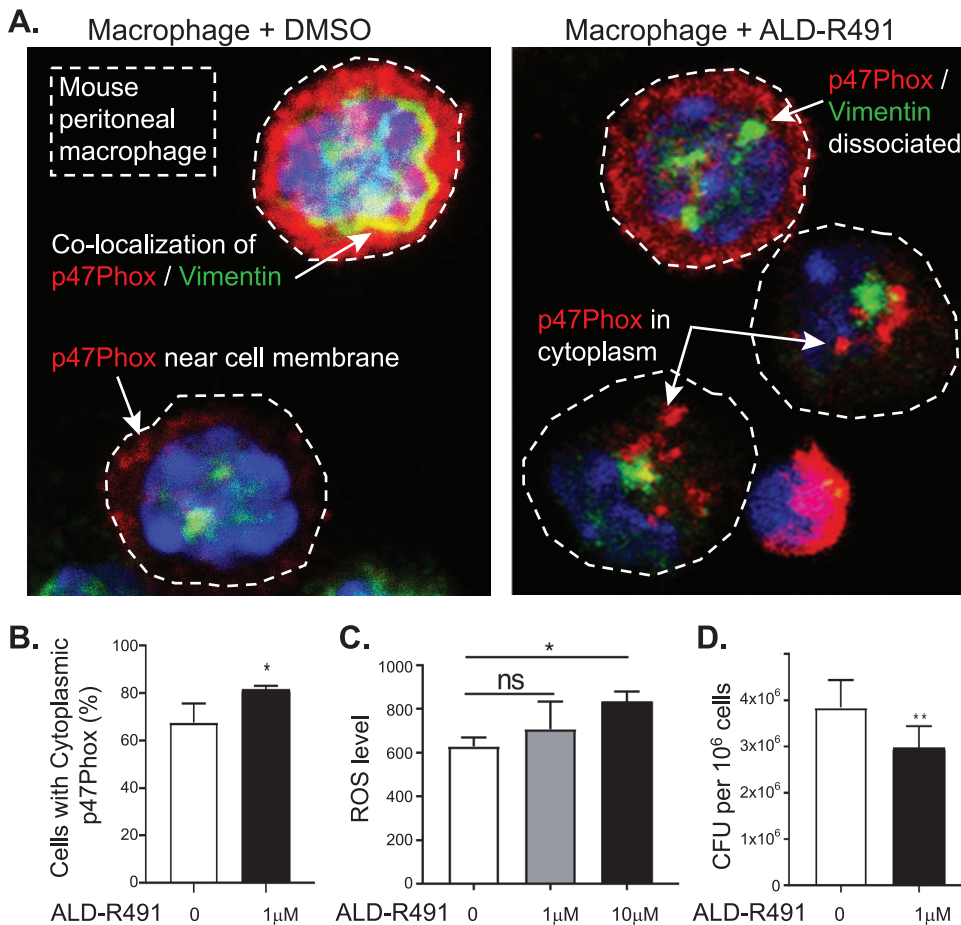


FIG 3 Effects of ALD-R491 on macrophages *in vitro*. (A and B) ALD-R491 dissociated vimentin from p47Phox of NADPH oxidase in mouse peritoneal macrophages; (A) Representative images of macrophages with or without ALD-R491 treatment; (B) Quantitation of p47Phox dissociated from vimentin from 3 independent experiments. (C) ALD-R491 increased cellular production of reactive oxygen species from Raw246.7 cells from three independent experiments. (D) ALD-R491 reduced the numbers of live *Salmonella* inside Raw246.7 cells, from six independent experiments. Two tailed *t* test. *, *P* < 0.05; **, *P* < 0.01.

limiting ROS production and consequently reducing the pathogen-killing efficiency of cells (30). In the mouse peritoneal macrophages, we found that p47Phox was abundantly present in the cell periphery next to the cell membrane and colocalized with vimentin. The vimentin-binding action of ALD-R491 caused a dissociation of vimentin from p47Phox and thereby increased the presence of p47Phox in the cytosol (Fig. 3A and B, Fig. S3), increased the production of ROS (Fig. 3C), and reduced the number of *Salmonella* organisms that survived in the macrophages by about 30% (Fig. 3D). These results suggest the potential of ALD-R491 to increase the pathogen-killing capacity of macrophages. As viral evasion of host immune surveillance is believed to play a major role in disease severity and persistence, the enhanced microcidal function of macrophage by ALD-R491 could reduce the ability of SARS-CoV-2 to survive once inside the macrophage, thereby decreasing the chance of viral persistence and preventing the escalation of inflammation and development of long-haul symptoms.

ALD-R491 directly activates regulatory T cells. In cases where the innate immunity fails to clear the pathogen, the adaptive immunity is then mobilized against the infection. Although this will help control infection, the overactive immune response is the most important contributor to morbidity and mortality in severe COVID-19. Among all immune cells, regulatory T cells (Tregs) are the key enforcers of immune homeostasis, marshalling many other immune cells in concert to keep inflammation in check. They prevent host tissues from damage from the pathogen-triggered excessive

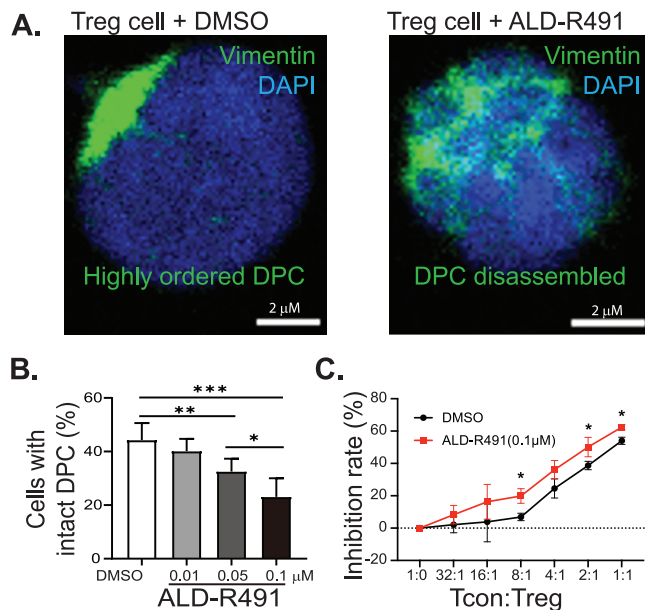


FIG 4 Effects of ALD-R491 on regulatory T cells *in vitro*. (A) ALD-R491 disassembled the distal pole complex (DPC) of mouse regulatory T cells. Representative images of Treg cells with or without ALD-R491 treatment. (B) Quantitative analysis of Treg cells with disassembled DPC, from three independent experiments. (C) Quantitative measurement of Treg cell activity, from three independent experiments. Two tailed *t* test. *, *P* < 0.05; **, *P* < 0.01; ***, *P* < 0.001.

antimicrobial immune responses and promote healing to repair epithelial damage and other tissue damage throughout the body. In severely ill COVID-19 patients, the levels of peripheral Tregs were found to be remarkably reduced (31–34), which has led to a call for Treg cell-based therapy (35) and a clinical trial (ClinicalTrials registration number NCT04468971) of infusions of Treg cells. Vimentin has been previously identified as forming the “mechanical” restraint structure inside regulatory T cells that regulates their switch between active and inactive status. Specifically, inside Tregs, the asymmetric partitioning of vimentin forms the distal pole complex (DPC), keeping the immunosuppressive molecules away from the immunological synapse that gets formed between Tregs and antigen-presenting cells, and thereby restraining the function of Treg cells (Fig. S3B) (21). We hypothesized that ALD-R491 would interrupt the DPC’s structural integrity and directly activate Tregs to increase their dampening and balancing actions, thereby addressing and potentially solving the cytokine storm of COVID-19. In cultured mouse Treg cells treated with ALD-R491 for a short period of time (2 h), concentrations as low as 0.01 μM resulted in a significantly decreased proportion of inactive Treg cells that had intact DPC (Fig. 4A and B). When disassembled, the DPC would release the immunosuppressive molecules, activating Treg cells. Indeed, a Treg suppression assay *in vitro* showed an increased Treg activity in the presence of ALD-R491 at a low concentration of 0.1 μM (Fig. 4C, Fig. S4). These results indicated that the highly ordered DPC structure was very sensitive to ALD-R491 and that Treg cells required very low concentrations of the compound to be activated.

Orally administered ALD-R491 shows therapeutic efficacy against SARS-CoV-2 infection in aged mice. Both macrophages and Tregs are highly heterogeneous and plastic, and their functions *in vivo* are largely context dependent. We focused on whether their enhanced functions by ALD-R491 observed *in vitro* would translate into therapeutic benefit against COVID-19 *in vivo*. To evaluate whether the oral compound would have exposure in the lung tissue at levels sufficient to be effective, we first measured the distribution of ALD-R491 in tissues after oral administration. In rats given ALD-R491 by gavage at 30 mg/kg, the compound was rapidly distributed in various tissues, with the highest exposure in the gastrointestinal tissues, as expected, enriched exposures in other tissues, including the lung and lymph nodes, and minimal exposure

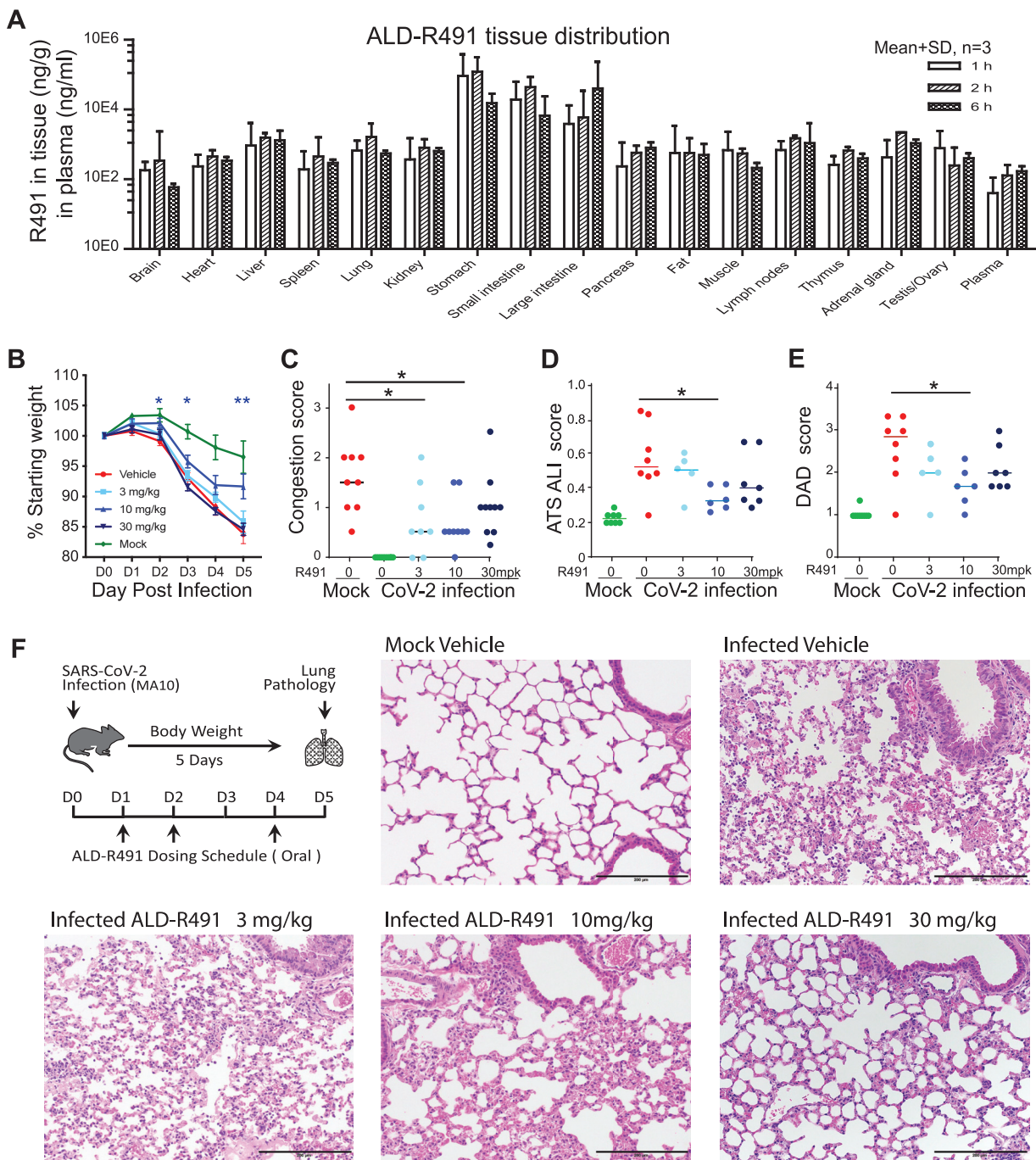


FIG 5 ALD-R491 tissue exposure in rats and therapeutic efficacy against SARS-CoV-2 infection in aged mice. (A) ALD-R491 concentrations were measured in the indicated tissues of female rats 1 h, 2 h, and 6 h after oral administration of the compound. (B to F) Therapeutic efficacy of ALD-R491 in aged BALB/c mice infected with SARS-CoV-2 M10. Body weights were measured daily over the course of study. Macroscopic and microscopic presentations of the lung at necropsy and in histopathology examination were blindly evaluated by a board-certified pathologist. The scores were compared between the infected vehicle group versus individual treatment groups. Two tailed *t* test; *, *P* < 0.05; **, *P* < 0.01. (B) Body weight change. (C) Lung congestion scores on day 5. (D) American Thoracic Society (ATS) acute lung injuries (ALI) scored by the method of Matute-Bello et al. (58). (E) The diffuse alveolar damage (DAD) scored by the method of Schmidt et al. (59). (F) Schematic presentation of the experimental protocol and representative images selected from mice with the ALI and DAD scores close to the scores of their group averages.

in the blood (Fig. 5A). The compound concentrations in the lung tissue 6 h after oral dosing maintained at levels as high as 1 μ M, which was a concentration more than sufficient for efficacy based on its effective concentrations *in vitro* (<0.1 μ M in multiple assays). These data provided the rationale for dose selection and supported a daily dosing treatment regimen.

Next, we tested the compound in a SARS-CoV-2 mouse-adapted (MA) model, in which the mutated SARS-CoV-2 virus can replicate in the upper and lower airways of both young adult and aged BALB/c mice. The model generates more severe disease in aged mice, reproducing the age-related increase in disease severity observed in humans (36). In this study, we utilized aged mice (11 to 12 months) to best mimic the most severe viral infection in the most vulnerable population in humans. The compound was orally administered prophylactically and therapeutically.

Prophylactic treatment had no effects under the study execution (Fig. S5A to F); however, therapeutic treatment showed significant efficacy in multiple measurements. Under the therapeutic protocol, the aged mice were administered the compound orally 1 day after the SARS-CoV-2 infection for 3 of the 5 study days on day 1 (D1), D2, and D4 and then sacrificed on D5. Therapeutic effects were observed more prominently in the medium-dose group of 10 mg/kg, as evidenced by reduced body weight loss over the course of the experiment (Fig. 5B), lower lung congestion as assessed macroscopically at the necropsy (Fig. 5C), milder lung tissue injury (Fig. 5D), and less diffuse alveolar damage (Fig. 5E) as evaluated microscopically in the histological examination. The lung tissues from mice in both the 10-and 30-mg/kg groups showed less inflammation and better-preserved alveolar structures (Fig. 5F). The viral loads in the lung tissues at the end of the study at D5 were at low levels with no difference among groups (Fig. S5F). The low viral titers at D5 were expected because in this model, without treatment, the viral loads in the lung were shown to peak at D2 and to decrease significantly by D4 (36). The viral titer at D5 in this study therefore was less meaningful in terms of antiviral efficacy since the virus in the surviving mice had been largely cleared regardless of treatment. The therapeutic efficacy seen *in vivo*, particularly given that only 3 doses were able to be administered relative to a 5-day course due to site constraints during the pandemic, was very significant both in its endpoints and in its short treatment regimen started after productive viral infection. With its dual actions of host-directed antiviral and antiinflammation, ALD-R491 represents a unique promising oral agent that is worth further investigation as a therapeutic against COVID-19.

Efficacy of ALD-R491 in treating and preventing lung injury and fibrosis in a rat model. With the therapeutic efficacy demonstrated in a COVID-19 animal model, we wanted to further evaluate whether the compound of multiple functions could be used to treat or prevent lung injury and the injury associated lung fibrosis. In COVID-19 patients with pneumonia or requiring intensive care, 42% or over 60% of them developed acute respiratory distress syndrome (ARDS) (37). Interstitial and intra-alveolar fibrosis are hallmarks of ARDS at advanced stages. Up to 25% of ARDS survivors develop physiologic evidence of lung fibrosis within 6 months. With the continuing rate of SARS-CoV-2 infection worldwide and the increasing populations of long hauler patients, an increase in lung fibrosis is expected in post-COVID-19 patients. Antifibrotic therapies have been proposed for treating severe COVID-19 patients and preventing fibrosis after SARS-CoV-2 infection (38); however, the available antifibrotic drugs are not well tolerated and would present especially high risk to COVID-19 patients. Vimentin is the major intermediate filament in fibroblasts, the cell type directly responsible for excessive collagen production and fibrosis. The roles of vimentin in tissue injury and fibrosis have been well established in the literature. Citrullinated vimentin mediates development and progression of lung fibrosis (39). Vimentin knockout (KO) or inhibition of vimentin has been shown to decrease collagen production (40), reduce lung injury, and protect the lung from developing fibrosis (22, 41).

We tested the vimentin-binding compound ALD-R491 in rats with bleomycin-induced lung fibrosis model, using prophylactic as well as therapeutic protocols. In both protocols, ALD-R491 significantly ameliorated lung tissue injury and lung fibrosis. Bleomycin directly injected intratracheally into to the unilateral lung caused massive lung injury and severe lung fibrosis. Compared with the positive-control treatment with BIBF1120 (nintedanib), a multiple tyrosine kinase inhibitor marketed as a first-line treatment for lung fibrosis, the treatment with ALD-R491 showed significantly improved body weight (Fig. 6A), indicating a superior safety profile of ALD-R491. Both

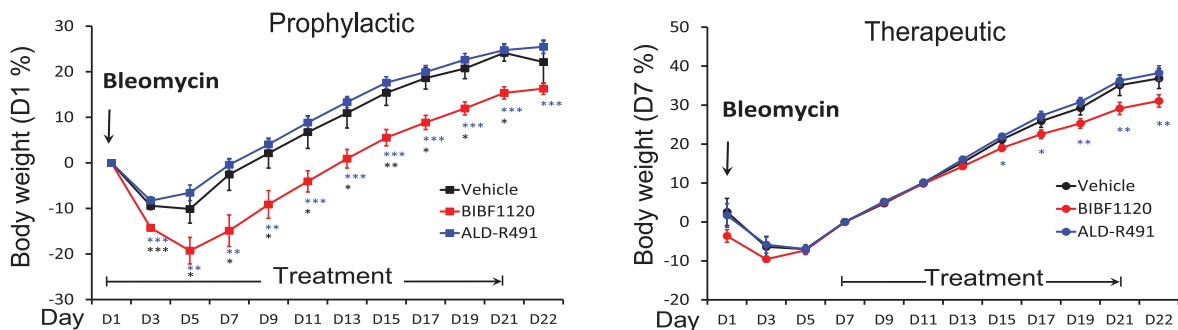
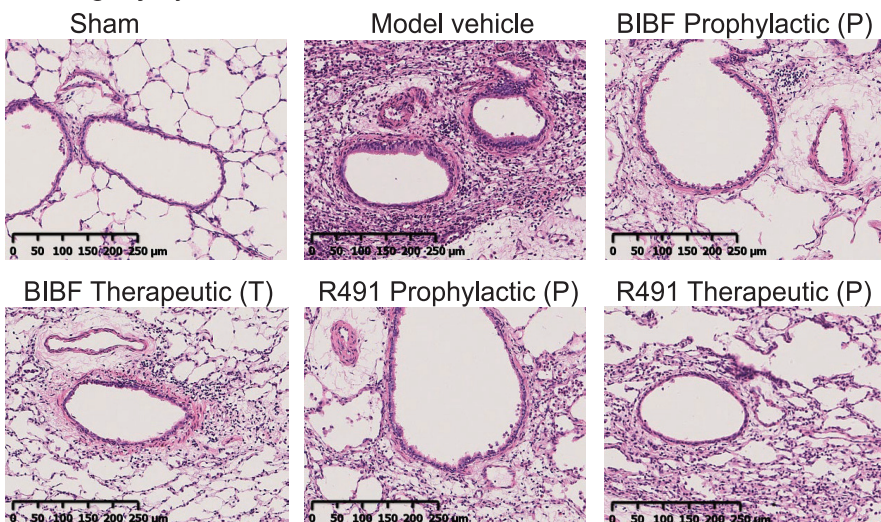
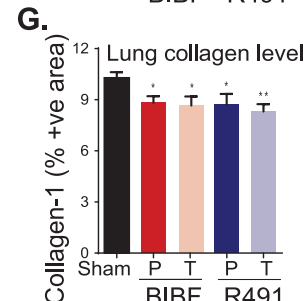
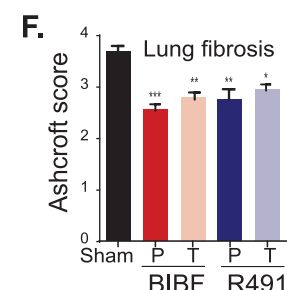
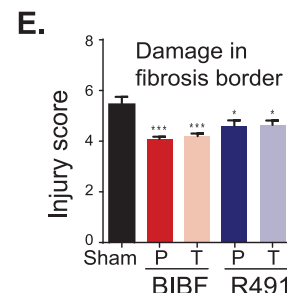
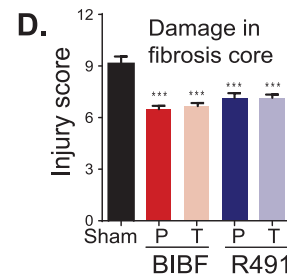
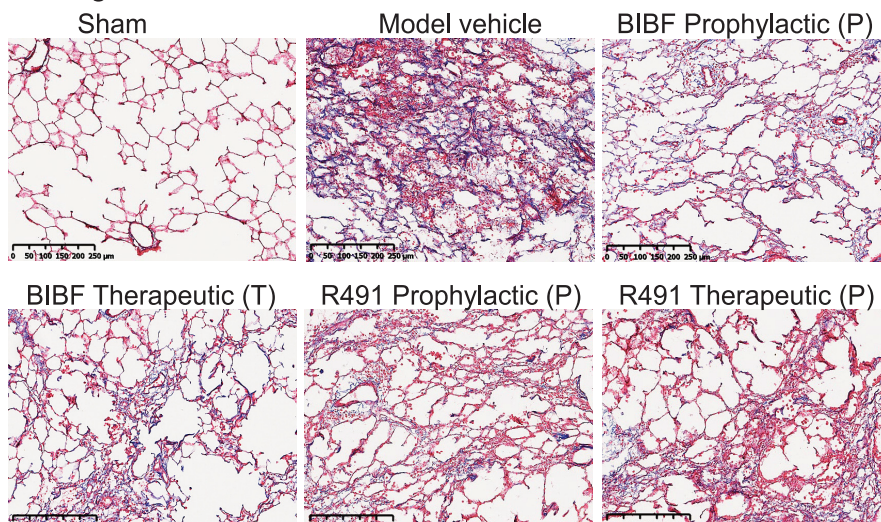
A. Body weight**B. Lung injury****C. Lung Fibrosis**

FIG 6 Efficacy of ALD-R491 in treating and preventing lung damage and fibrosis. (A) Body weight change. The percentage of body weight change was calculated based on the body weight measured on the day when ALD-R491 treatment started. *, P < 0.05; **, P < 0.01; ***, P < 0.001 versus model vehicle. (B) Images for bronchial and arteriole injury in the fibrotic core (C) Images for alveolar fibrosis. The left lungs were stained with Masson's trichrome. Blue color, collagen; light red or pink color, cytoplasm; dark brown, cell nuclei. (D) Bronchial and arteriole injury in the fibrotic core. (E) Bronchial and arteriole injury in fibrotic border. (F) Lung fibrosis. The Masson's trichrome-stained lung sections were scored according to Ashcraft scoring criteria. (G) Quantitative measurement of collagen-1-positive areas in lung fibrotic tissue section. The percentages of collagen-positive area for each treatment group were compared with that for the model vehicle group. Two-tailed t test; *, P < 0.05; **, P < 0.01; ***, P < 0.001. n = 9.

therapeutic and prophylactic treatment using ALD-R491 reduced bronchial and arteriole injury in the fibrotic core (Fig. 6B and D) and the fibrotic border (Fig. 6E, Fig. S6A) and reduced damage and fibrosis in alveoli (Fig. S6B, Fig. 6C and F). Interestingly, careful examination revealed that the Masson's trichrome images for samples with comparable Ashcroft scores exhibited a remarkable difference in connective tissue staining between the BIBF1120 and ALD-R491 groups, i.e., the ALD-R491 group had a much less intense blue color (stains for fibrosis) than the BIBF1120 group had (Fig. 6C). This result indicates that, when assigned comparable Ashcroft scores, the lung tissues from ALD-R491-treated animals had less fibers than the lung tissues from BIBF1120-treated animals, so the Ashcroft scoring on lung fibrosis for ALD-R491 failed to capture this improvement in visible histopathology (less blue) because it falls outside the density rubric of the Ashcroft scoring matrix (scores only density, not color). This discrepancy was further confirmed by collagen-I immunohistochemistry (IHC) staining, which showed the actual reduction in fibrosis measured by collagen-I deposition was more significant than that by Ashcroft score in the lung of mice treated with ALD-R491. Compared with the vehicle control, both ALD-R491 and BIBF1120 reduced collagen-I deposition in the lung fibrosis core, with the reduction of collagen more significant in the ALD-R491 group than in the BIBF1120 group (Fig. 6G, Fig. S6C). This was consistent with the markable difference in amounts of fibers (blue color) seen with Masson's staining but not reflected by Ashcroft scores (Fig. 6C). Although Ashcroft scoring underestimated the efficacy of ALD-R491 in reducing fibrosis, the results from all the evaluation criteria indicate that ALD-R491 has a superior safety profile and a therapeutic potential not only in ameliorating lung injury but also in preventing and treating lung fibrosis, all of which is directly relevant to use in COVID-19 and its complications.

DISCUSSION

To address the multifaceted pathogenesis of SARS-CoV-2 infection, we are developing a new therapeutic agent with both antiviral and anti-inflammatory action by binding to vimentin (Fig. 7). This first-in-class mechanism of action is fundamentally different from that of any existing pipeline agent, or any repurposed drug (13, 42). Importantly, the antiviral mechanisms of ALD-R491 create multiple novel actions against viral infection—first, a blockade of spike protein and ACE2-mediated endocytosis and of endosomal trafficking and exosomal release, which are the cellular processes that are unlikely to be evaded by the virus even with mutations, and second, an enhanced ability of macrophages to kill pathogens, which is critical both for containing the viral spread at early stages and for clearing persistent viral presence after the acute phase of infection. The anti-inflammatory mechanisms of ALD-R491 could also create multiple actions that are novel and different from existing agents and highly sought after for their specific potential against the hyperinflammation of COVID-19—a direct Treg activation, as shown in this study, and a potential inhibition of NLRP3 inflammasome activation, as a previous study suggested (22). The therapeutic effects of the compound on the aged mice with a full-blown, ongoing SARS-CoV-2 infection is not only a proxy for its efficacy against severe disease, but also informs its use in the elderly and fragile, two groups of COVID-19 patients with the most concerning unmet need. The therapeutic and preventive effects of the compound on lung injury and fibrosis make it also applicable to patients with post-COVID-19 complications. With oral administration, ALD-R491 can be conveniently dosed and broadly accessible to non-hospitalized patients, a population that is growing rapidly as this first pandemic matures.

These remarkable actions can take place because the pathogenesis of SARS-CoV-2 infection involves multiple cellular processes in various types of cells where vimentin is abundantly expressed, including the pulmonary alveolar epithelial cells (AT1 and AT2 cells), vascular endothelial cells, fibroblasts, macrophages, and regulatory T cells (43, 44).

The binding of ALD-R491 to vimentin altered the organization and dynamism of the filaments (Fig. 1A and B), which impacted multiple cellular processes in the cells

Disease uses vimentin in multiple ways:

One target can achieve multiple actions against multiple aspects of COVID-19

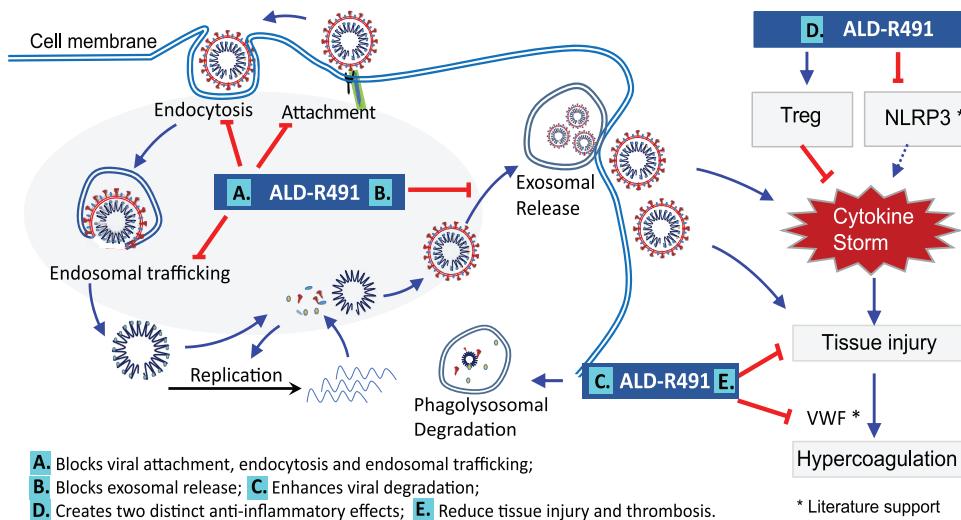


FIG 7 Schematic presentation of actions of ALD-R491 in COVID-19. (Left) The subcellular events in a cell being infected by a SARS-CoV-2 virus and the host-directed antiviral actions of ALD-R491. (Right) The anti-inflammatory actions of ALD-R491. Both suppressing NLRP3 inflammasome and activating Tregs would dampen cytokine storm and subsequent tissue damage. Curved blue arrows and the shaded oval area highlight SARS-CoV-2 infection processes. Straight blue arrows indicate positive regulation, and red blunt-ended arrows, negative regulation. Treg, regulatory T cell; NLRP3, NLR family pyrin domain containing 3 inflammasome; VWF, Von Willebrand factor; *, action of vimentin described in literature but not tested in this study.

(Fig. 1D to F), leading to a blockade of the initial steps of SARS-CoV-2. Vimentin can function as an attachment receptor on the cell surface and assist membrane and vesicle transport at both anterograde and retrograde directions inside the cell (45, 46). It appears to be widely hijacked by viruses for facilitating their infection, as seen with both SARS-CoV (47) and SARS-CoV-2 (48). Our study showed that ALD-R491 potently inhibited Spike protein-ACE2-mediated viral entry through a blockade of endocytosis, the first step of the viral infection (Fig. 2). It has been demonstrated that newly assembled SARS-CoV-2 particles in the host cell, rather than budding to exit, egress from the cells by fusing a multiple-vesicle body (MVB)-like structure with the cell membrane, resembling exosomal or lysosomal release pathways (27, 49). Our study showed that vimentin regulated exosomal pathways (25) and that ALD-R491 dose-dependently inhibited exosome release (Fig. 1F), which could lead to a blockade of the viral egress. All these actions contribute to a multipart host-directed antiviral mechanism that offers a multipart blockage of the transportation machinery hijacked by viruses for productive infection. As the compound acts on cellular processes, not the virus itself, it therefore applies to all the SARS viruses regardless of strains or mutations, which is especially advantageous because of the rapid evolution of current SARS-CoV-2 and the potential for future outbreaks of other coronaviruses.

ALD-R491's ability to enhance microcidal activity of macrophages is critical not only for controlling the infection but also for reducing the virus-triggered escalation in inflammation. Monocytes and macrophages are phagocytic innate immune cells present in the circulation and in the tissues, respectively, serving as the first line of defense upon encountering pathogens. Macrophage infiltration in alveoli is a hallmark of COVID-19 (44). Alveolar macrophages express the ACE2 and TMPRSS2 genes that help the cells recognize and internalize SARS-CoV-2. The positive and negative transcripts of SARS-CoV-2 have been detected or enriched in alveolar macrophages, monocytes, and peripheral blood mononuclear cells (PBMCs) in COVID-19 patients (29, 43), suggesting the existence of live SARS-CoV-2 in the monocytes and macrophages. The

S1 protein of SARS-CoV-2 has been found persistently present in CD16⁺ monocytes of post-COVID-19 patients for more than a year (50), suggesting the failure of monocytes to clear the virus. It remains to be investigated whether monocytes and macrophages can support active replication of SARS-CoV-2, as has been reported for SARS-CoV and Middle East respiratory syndrome coronavirus (MERS-CoV). Regardless, monocytes and macrophages may still serve as a permissive system and/or as a viral reservoir, both of which are known to enable virus to spread to other tissues or anchor specifically within the pulmonary parenchyma (51–53), especially when there is a long duration between the onset of symptoms and the development of respiratory failure (6 to 12 days) or a prolonged course (several months or longer) of syndromes in COVID-19 long-haulers (54). Compromised ability of monocytes and macrophages to clear pathogens in COVID-19 patients might lead to the persistence of the virus inside the cells, escalating a proinflammatory response during the acute phase and recurring injuries and lingering symptoms in the postacute phase. Enhancing the ability of macrophages to clear pathogens (Fig. 3A and B, Fig. S3), ALD-R491 could therefore be one of ALD-R491's most distinct, significant, and unique therapeutic benefits in patients with COVID-19 as well as with post-COVID-19 syndromes.

Direct Treg activation is a unique feature of ALD-R491 (Fig. 4, Fig. S4). The binding of ALD-R491 to vimentin physically disassembles DPC and, therefore, directly activates Tregs. This activation occurs rapidly (less than 2 h), unlike other Treg-activating mechanisms that require changes in signaling pathway or gene expression, which are indirect and slow-acting in nature. For COVID-19, with its rapid disease progression, prompt intervention appears to be especially important, which makes the fast-acting ALD-R491 advantageous. In addition, Treg activation via vimentin targeting was shown not to alter homeostasis of Tregs (55) and therefore would not cause general immunosuppression, which makes it fundamentally different from the use of steroids. Separated from its immune-related functions, Treg activation has been shown to have a major direct and nonredundant role in tissue repair and maintenance (56). Through directly activating Tregs and other mechanisms, ALD-R491 could not only dampen the overactive immune system without compromising its antiviral response, but also prevent tissues from damage and facilitate their repair. Reduced tissue injury by ALD-R491 has been consistently observed in our studies across different animal models (Fig. 5 and 6).

The antifibrosis activity of ALD-R491 is a further additive to a complete view of its impact on COVID-19. Lung pathologies from COVID-19 patients and computed tomography scans of the chest in post-COVID-19 patients showed a significant increase in fibrosis score (44). Fibroblasts are the primary mesenchymal cells in lung tissues. Overactivation of fibroblasts is the direct cause of lung fibrosis. Alveolar fibroblasts in acute lung injury (ALI) and acute respiratory distress syndrome (ARDS) exhibit a persistent activated phenotype with enhanced migratory and collagen-1 production capacities. Vimentin is the major intermediate filament protein in fibroblasts, promoting the motility and invasiveness of cell and the production of collagen (40). Targeting vimentin has been shown to be effective in reducing lung fibrosis (22, 41). As lung fibrosis can develop and persist in patients that have recovered from severe COVID-19 (57), the antifibrotic activity of ALD-R491 (Fig. 6) should provide additional values against COVID-19 and its complications.

In summary, the vimentin-binding compound ALD-R491 impacts multiple cellular processes as well as various types of cells that are involved in the pathogenesis of COVID-19. Its multipart host-directed antiviral and anti-inflammatory actions and its broad preclinical efficacy make the compound a promising drug candidate worth further development and exploration for the treatment of COVID-19 and other related diseases.

MATERIALS AND METHODS

The compound. The vimentin-binding compound used in this study was ALD-R491, (E)-1-(4-fluorophenyl)-3-(4-(4-(morpholine-1-yl)-6-styryl-1, 3, 5-triazinyl-2-amino) phenyl) urea. It has a molecular formula of C28H26FN7O2 and a purity of >98%. The compound was synthesized at Bellen Chemistry Co.,

Ltd., analyzed at Porton Pharma Solutions, Ltd., and provided by Luoda Biosciences, Inc., and Aluda Pharmaceuticals, Inc.

Endocytosis and endosomal trafficking. HEK293T cells were purchased from The Cell Bank of Type Culture Collection of Chinese Academy of Sciences (Shanghai, China); plasmid pMAX-GFP, from Lonza; transfection agent Lipofectamine 2000, from Invitrogen. The cells were grown in 96-well plates to approximately 70% confluence after overnight culture and transfected in 6 replicates with pMAX-GFP plasmid DNA (0.6 µg per well) using Lipofectamine 2000 according to the manufacturer's instructions. The media were changed at 4 h posttransfection, and then the culture plates were placed in an IncuCyte system (Essen Bioscience) for live cell imaging under a ×10 lens objective. The fluorescence intensity (GFP signals) in each well was captured once every 2 h continuously until the end of the experiment.

Exosomal release. Quantification of exosome release using the ExoHPTM platform. Supernatant (around 98 µl) was collected from each well of the cultured cells and then centrifuged at 300 × g for 10 min to remove cells and at 2,000 × g for 20 min and 10,000 × g for 30 min to remove apoptotic bodies and large extracellular vesicles. Exosomes were isolated from these processed supernatants with an ExoEZ exosome isolation kit (no. ExoCC50; Evomim Science, Sunnyvale, CA) according to the manufacturer's instructions. Luciferase activity in 50 µl of exosome suspension was measured with a Promega Renilla luciferase assay kit (no. E2810; Madison, WI) in TECAN Infinite M100 (TECAN, San Jose, CA).

Measurement of nanoparticle size, concentration, and distribution with nanoparticle tracking analysis (NTA). Overnight-cultured Huh7NC12 at 70% confluence was treated for 2 days with medium consisting of dimethyl sulfoxide (DMSO) and the indicated concentrations of compounds. Then, culture supernatants were collected, centrifuged at 300 × g for 10 min and 2,000 × g for 20 min to remove cells, cell debris, and apoptotic bodies (pellet 1) and at 10,000 × g for 30 min to remove large extracellular vesicles (pellet 2). Exosomes were isolated from these processed supernatants by ultracentrifugation (100,000 × g for 90 min) (pellet 3). The isolated exosomes from 5 ml or 10 ml of supernatants (pellet 3) were suspended in 1 ml phosphate-buffered saline (PBS) and visualized on the NanoSight 300 instrument (NanoSight Ltd, Amesbury, UK). The analysis setting was kept constant between samples. The size and number of nanoparticles were calculated.

Pseudoviral infection. HEK293T/hACE2 cells, Pseudovirus-2019-nCoV-GFP-IRES-LUC and control Pseudovirus-GFP-IRES-LUC were purchased from FUBIO (Suzhou, China). The cells were seeded into 96-well plates at 1 × 10E4 cells per well, cultured until 40% confluence, and mock-infected or infected with the pseudovirus (2 × 10E7 transforming units [TFU]/ml) at an MOI of 0.5, 5, and 50, respectively. The cells were exposed to NH4Cl as the positive control, DMSO as the negative control, and ALD-R491 at concentrations of 0.01, 0.0316, 0.1, 0.316, 1, 3.16, and 10 µM for a period from 2 h right before the infection to the start of the infection (before infection), for the whole experiment period from 2 h before the infection to the end of the experiment (full-time), or for a period from 2 h after the start of the infection to the end of the experiment (after infection). About 12 h after the infection, the virus-containing media were removed and replaced with each fresh conditional medium, and then the culture plates were placed in the IncuCyte system (Essen Bioscience) for live cell imaging under a ×10 lens objective. The fluorescence intensity (GFP signal) in each well was captured once every 2 h continuously for 48 h, and then the cells were measured for luminescence signal using a BioTek Synergy 4 plate reader. The viability of mock-infected cells treated with ALD-R491 at different concentrations was measured with an MTT assay kit (Beyotime). Each treatment condition was performed in triplicate ($n = 3$).

Monocyte/macrophage functions. The killing of *Salmonella* by Raw264.7 cells. The cells in a 24-well plate were incubated with ALD-R491 at 1 µM for 2 h. The cells were counted and then added with *Salmonella enterica* serovar Typhimurium (SL1344) to make the ratio of cells to *Salmonella* 1:10. The culture was gently shaken and then centrifuged at 1,000 rpm for 5 min. The cells were incubated in an incubator for 30 min, washed 3 times with PBS, and then cultured for 1 h in Dulbecco modified Eagle medium (DMEM) medium containing gentamicin at 50 µg/ml. The cells were then lysed with 1% Triton X-100, and the lysates were serially diluted and plated on *salmonella*-shigella (SS) plates for 24 h. The bacterial colonies were counted. Six independent experiments were performed.

Preparation of mouse peritoneal macrophages. Mice were intraperitoneally injected with 1 ml of 4% Brewer's modified thioglycolate medium Brewer Modified (BD, USA). Four days later, the mice were sacrificed with cervical dislocation and soaked in 75% alcohol for 3 min. The abdominal skin was cut open to fully expose the peritoneum. The peritoneum was lifted with ophthalmic forceps and injected with 8 ml of pre-cooled PBS into the abdominal cavity. The mouse abdomen was gently massaged for 5 min, and the fluid was withdrawn from the abdominal cavity with a syringe, transferred into a 15-ml centrifuge tube, and centrifuged at 4°C, 1,000 rpm for 10 min. The pelleted cells were resuspended with RPMI 1640 medium and inoculated in a 24-well plate containing round slides. After culturing in an incubator for 2 h, the cells were washed with PBS three times and replaced with a new medium.

Dissociation of p47phox and vimentin by ALD-R491 in macrophages. The peritoneal macrophages were incubated in the presence of lipopolysaccharide (LPS) (5 µg/ml) overnight and then treated with ALD-R491 (1 µM) for 2 h, fixed with 1% paraformaldehyde (PFA) for 10 min, washed with PBS three times, permeabilized with 0.2% Triton X-100 for 10 min, washed with PBS three times, blocked with serum for 30 min, and washed with PBS again three times. The cells were incubated overnight at 4°C with the anti-p47phox primary antibody (Santa Cruz Biotechnology; sc-17844) and the anti-vimentin primary antibody (Santa Cruz Biotechnology; sc-5565). After being washed three times with PBS, the cells were incubated with the secondary antibody for 1 h in the dark at room temperature. The cells were further stained with DAPI (4',6-diamidino-2-phenylindole) for nuclei, washed with PBS three times, and then mounted. The cells were examined under a confocal microscope, and images were taken from three separate fields. Cells with p47phox at locations near the cell membrane or/and in the cytoplasm away from

cell membrane were counted. The number of the cells with p47phox in the cytoplasm away from the cell periphery was counted from samples treated with DMSO or ALD-R491, and percentages of cells with cytoplasmic p47phox were calculated. Three independent experiments were performed.

Cellular ROS measurement. Raw264.7 cells were seeded into a 12-well plate and cultured until 90% confluence and then added with ALD-R491 at different concentrations and incubated for another 2 h. DCFH-DA (Beyotime; S0033S) was diluted 1:1,000 with serum-free culture medium to the final concentration of 10 μM and then added to the 12-well plate and incubated for 30 min. The cells were washed twice with PBS, harvested after digestion, and transferred into a 96-well plate. The fluorescence intensity was measured in a microplate reader using the excitation wavelength of 488 nm and the emission wavelength of 525 nm.

Treg activation. Preparation of CD4⁺CD25⁺/ cells. CD4⁺ T cells were isolated from spleen of BALB/c mice (6 to 8 weeks old) by microbeads according to the manufacturer's instructions. Briefly, single-cell suspensions from mouse spleen were incubated with anti-CD4-biotin antibody (BioLegend; 100508) and then streptavidin microbeads (Miltenyi; 130-048-102). Labeled CD4⁺ cells were positively isolated using LS columns and a Quadramacs separator. Then the CD4⁺ T cells were stained with anti-CD4-APC (BioLegend; 100412) and anti-CD25-PerCP-CY5.5 (BD; 551071) flow cytometry antibodies. Conventional T cell populations (Tcon; CD4⁺CD25⁻), and regulatory T cell populations (Treg, CD4⁺CD25⁺) were isolated with a BD FACS Aria III system.

Distal pole complex in Treg cells. The isolated Treg cells (CD4⁺CD25⁺) were incubated in RPMI complete culture medium with DMSO or ALD-R491 for 2 h at 37°C. Then the treated Treg cells were collected for immunofluorescence assay. Briefly, the Treg cells were fixed for 30 min in 4% PFA and permeabilized for 5 min with 0.2% Triton X-100 in PBS. The permeabilized cells were blocked with 3% bovine serum albumin (BSA) for 1 h and incubated with anti-vimentin primary antibody (Proteintech; 10366-1-AP; 1:200) overnight at 4°C. Then, the cells were incubated with AF488 labeled secondary antibody (SouthernBiotech; 4050-30; 1:500), followed by incubation with DAPI (Roche; 10236276001). Each sample was imaged on a Nikon A1 confocal microscope for at least three separate fields.

Treg function assay. To assess Treg suppressive function, Tcons were labeled with carboxyfluorescein succinimidyl ester (CFSE; Invitrogen; 65-0850-84) and then cocultured with Tregs (pretreated with or without ALD-R491) in different ratios in a 96-well plate for 3 days. T cells were activated by coated-CD3 antibody (BioLegend; 100302) and diluted CD28 antibody (BioLegend; 102102) with or without ALD-R491. After 3 days, cells were collected for fluorescence-activated cell sorter (FACS) analysis on a BD FACS Canto II. FACS data were analyzed using FlowJo software (TreeStar). The inhibition of Treg cells on Tcon activation was quantified. Three independent experiments were performed.

Tissue distribution in rats. Animals and housing. Sprague-Dawley rats of specific-pathogen-free (SPF) grades at ages of 6 to 8 weeks were purchased from Beijing Vital River Laboratory Animal Technology Co. Ltd., with animal certificate no. SCXK (Jing) 2016-0006 and with animal quality certificate no. 1100112011030349 and no. 1100112011030350. Animals were housed in the animal facility at Joinn Laboratories (Suzhou, China) with 5 or fewer rats per gender in each polycarbonate cage and in an environmentally monitored, well-ventilated room (SPF grade) maintained at a temperature of 20 to 26°C and a relative humidity of 40% to 70%. Fluorescent lighting provided illumination in an approximately 12-h light/dark cycle per day. A total of 18 rats (9/gender) were used in the study. Only data from the 9 female animals (3 animals per time point) are presented.

Experiment procedures, data acquisition, and analysis. The 9 female rats in 3 groups, with body weights from 195 to 214 g, were orally administered ALD-R491 at 30 mg/10 ml/kg. At 1, 2, and 6 h after drug administration, one group of the animals was anesthetized and then euthanized using abdominal aorta exsanguinations, and their blood and tissue samples were taken. The concentrations of ALD-R491 in rat plasma, tissue, feces, urine, and bile samples were analyzed by the validated liquid chromatography tandem mass spectrometry (LC-MS/MS) methods with the LLOQ (lower limit of quantification) concentrations of 0.500 ng/ml for plasma and 0.500 ng/ml (equal to 25.0 ng/g after conversion) for tissue. The concentration value below the LLOQ was set as 0 for the purpose of calculation. LabSolutions software (version 6.81 SP1) from Shimadzu Company was used for outputting raw chromatograms and generating concentration and accuracy results of the plasma samples. WinNonlin was used for distribution data statistical analysis (including mean, standard deviation [SD], and percentage coefficient of variation [CV]) of plasma and tissues concentrations. Microsoft Office Excel (2007) was used for tissue concentration column graphs.

SARS-CoV-2 M10 infection in aged mice. Animals and housing. Aged (11- to 12-month-old) female BALB/c mice were obtained from Envigo (retired breeders). The animals were housed in the animal facility at the University of North Carolina, Chapel Hill, NC, with 5 mice in each cage with food and water provided *ad libitum*, with a 12 h/12 h light/dark cycle. The animals were acclimated for 7 days in the biosafety level 3 (BSL-3) facility prior to any experimentation.

Virus and model establishment. Baric laboratory generated the stock of SARS-CoV-2 MA10, a mouse-adapted virulent mutant created from a recombinantly derived synthesized sequence of the Washington strain. The virus was maintained at low passage (P2-P3) to prevent the accumulation of additional potentially confounding mutations. Mice were anesthetized intraperitoneally (i.p.) with a combination of 50 mg/kg ketamine and 15 mg/kg xylazine in 50 μl and then infected intranasally (i.n.) with 10³ PFU of sequence- and titer-verified SARS-CoV-2 MA10 in 50 μl of DMEM diluted in PBS to the inoculation dosage.

Experiment groups and treatment regimens. A total of 80 animals were used in this study. Ten animals per group were randomly assigned in 1 mock-infected vehicle treatment group and 7 virus (10³ PFU SARS-CoV-2 MA10)-infected groups treated orally (p.o.) via gavage with vehicle and ALD-R491, respectively, at 3, 10, and 30 mg/kg in prophylactic protocol (dosing at -15, -5, +24, +48, +72, and +96 h postinfection) or therapeutic protocol (dosing at +24, +48, and +96 h postinfection).

Procedure and endpoint. Daily clinical evaluation and scoring were performed, including body weight and symptoms. The animals that survived anesthesia were carried to the experimental endpoint. As the mice were continuing to lose weight at all doses and in both treatment arms and the disease scores were increasing, all animals were euthanized at 5 days postinfection. Euthanasia was performed by inhalational isoflurane (drop method) and thoracotomy, with removal of vital organs (lungs). Lung tissue was taken for assessments of titer, RNA, and histology. Serum was taken for downstream analysis.

Histopathological examination of the lung. Lung specimens were fixed in formalin and stained with hematoxylin and eosin for histological assessments. Lung samples were scored by a board-certified veterinary pathologist for acute lung injury (ALI) and diffuse alveolar damage (DAD). The ATS ALI score is a weighted composite score based on the Matute-Bello rubric and considers neutrophils in the alveolar space, neutrophils in the interstitium, hyaline membrane formation, protein in airspaces, and alveolar septal thickening. All lung specimens were submitted for scoring; the pathologist scored all specimens that were deemed suitable. Thus, at least 6 lungs were scored under all conditions.

Statistical analyses were performed by Kruskal-Wallis test (titer), one-way analysis of variance (ANOVA) (congestion score), or two-tailed *t* test (weight loss, American Thoracic Society [ATS] ALI, and DAD scores).

Bleomycin-induced lung injury and fibrosis in rats. Animals and housing. A total of 45 male SD rats of SPF grade were purchased from Beijing Vital River Laboratory Animal Technology Co., Ltd., with the company certificate no. SCXX (Jing) 2012-001 and the animal use certificate no. 33000800003683. The animals were housed in the Animal House Facility of KCI Biotech (Suzhou, China), Inc., at a temperature of 20 to 26°C and a relative humidity of 40% to 70%. Fluorescent lighting was provided at approximately a 12 h light/dark cycle per day. The experimental protocol was reviewed and approved by the Institutional Animal Care and Use Committee (IACUC) at KCI Biotech, Inc. All experimental procedures were conducted in conformity with the institutional guidelines issued by KCI Biotech, Inc.

Model establishment. This study was carried out in strict accordance with the standard operating procedure (SOP) institutional guidelines for the care and use of laboratory animals. The rats were anesthetized by intraperitoneal injection of pentobarbital sodium at a dose of 50 mg/kg. The skin in the neck area was disinfected, and then the skin layers were carefully incised to have the trachea exposed. Bleomycin (BLM) was directly injected into left main bronchus at a dose of 3 mg/kg body weight in a volume of 1.0 ml/kg via a cannula. After the skin layers were closed, the animals were placed on an electric heat pad at 37°C until they woke up from anesthesia before being returned to holding cages with free access to water and diet.

Experiment groups and treatment regimen. The modeled rats were randomly assigned to 5 groups ($n = 9$ per group), treated p.o. via gavage, respectively, with vehicle at 5 ml/kg/day, with BIBF1120 at 100 mg/kg/day prophylactically (q.d.; from day 1 to day 21) or therapeutically (q.d.; from day 8 to day 21), and with ALD-R491 at 100 mg/kg/day prophylactically (q.d., from day 1 to day 21) or therapeutically (q.d.; from day 8 to day 21). One day after the last dosing (day 22), all animals were euthanized according to the standard SOP at KCI Biotech. The animals were perfused systemically with ice-cold saline, and their left lungs were harvested and perfuse-fixed with 10% formaldehyde solution (3 ml of each lung) and then processed for pathological analysis.

Histopathological examination of the left lungs. The whole left lung was dehydrated and embedded in paraffin wax. The sections were cut at a thickness of 4 μ m and processed for hematoxylin and eosin (H&E) and Masson's trichrome staining. All the procedures were performed according to KCI pathology SOPs. Whole slides were then scanned with a Hamamatsu NanoZoomer digital pathology S210 slide scanner after staining.

Bronchiole and pulmonary arteriole damage and inflammatory cell infiltration in fibrosis core and fibrosis border areas were scored with H&E-stained slides.

Criteria for grading the damage of the terminal bronchiole wall were score 0 for normal structure; score 1 for normal structure with less than 1/2 of the terminal bronchiole wall area injury and characterized by bronchial epithelial cells damage and epithelium regeneration, wall edema, medium layer of the mucosal muscle degeneration or regeneration; score 2 for structure with more than 1/2 of the terminal bronchiole wall area injured and characterized by bronchial epithelial cell damage and epithelium regeneration, wall edema, medium layer of the mucosal muscle degeneration or regeneration; and score 3 for structure with more than 1/2 area of the terminal bronchiole wall injured and characterized by bronchial epithelial cell damage and epithelium regeneration, wall edema, medium layer of the mucosal muscle degeneration or regeneration, granulomas formation or fibrosis.

Criteria for grading inflammatory cell infiltration in the terminal bronchiole wall were score 0 for normal structure with no inflammatory cell infiltration; score 1 for a few scattered but localized inflammatory cell infiltrations (fewer than 10 cells per field) in the outer wall of the terminal bronchiole; score 2 for numerous scattered inflammatory cell infiltrations that were focal or diffuse, affecting less than 1/2 of the total area of the terminal bronchiole wall; score 3 for diffuse infiltration of inflammatory cells that affected more than 1/2 of the total area of the terminal bronchiole wall and extended to the inner and the medium layers of basement membrane.

Criteria for grading the damage of pulmonary small arteries wall were score 0 for the clear and complete structure of pulmonary small arteries; score 1 for partially exfoliated endothelial cells; score 2 for exfoliated endothelial cells with degeneration, regeneration, or small focal necrosis in the medium layer of smooth muscle; score 3 for exfoliated endothelial cells with degeneration, regeneration, or small focal necrosis and formation of granulomas or fibrosis.

Criteria for grading inflammatory cell infiltration in the pulmonary arteriole were score 0 for normal structure of pulmonary small arteries; score 1 for a few scattered and localized inflammatory cell infiltrations (fewer than 10 cells per field) in the outer wall of pulmonary small arteries; score 2 for numerous

scattered inflammatory cell infiltrations, affecting less than 1/2 of the total area of the outer wall of pulmonary small arteries; score 3 for diffuse infiltration of inflammatory cells that affected more than 1/2 of the total area of the pulmonary small artery wall and extended to the medium layer of the basement membrane.

BLM-induced left lung injury and fibrosis were evaluated with Masson trichrome-stained slides using the Ashcroft scoring matrix. The criteria were score 0 for the normal structure with no fibrotic lesion in alveolar septum; score 1 for the isolated and simple pulmonary fibrosis in alveolar septum (alveolar walls thicker but are thinner than triple that for a normal lung) and little exudate and no fibrosis material in major alveolar areas; score 2 for the clear fibrosis change in alveolar septum (alveolar walls thicker than triple that for a normal lung) with formation of small nodules that were not connected and little exudate and no fibrosis material in major alveolar areas; score 3 for the formation of early stage fibrosis forms in all alveoli in alveolar septum (alveolar walls thicker than triple that for a normal lung) and little exudate and no fibrosis material in major alveolar areas; score 4 for the lung fibrosis with alveolar septum still visible and the formation of isolated fibrosis nodules in alveolar areas ($\leq 10\%$ at high magnification); score 5 for the lung fibrosis with alveolar septum still visible, the formation of integrated fibrosis nodule in alveolar areas ($> 10\%$ and $\leq 50\%$ at high magnification), and the lung structure substantially impaired but still present; score 6 for the seen but barely existing alveolar septum and the formation of integrated fibrosis nodule in alveolar areas ($> 50\%$ at high magnification) and the lung structure barely existing; score 7 for the disappeared alveolar septum and the pulmonary alveoli and interstitial fibrosis proliferation seen but still with vacuole structures; score 8 for the disappeared alveolar septum and the pulmonary alveoli and interstitial fibrosis proliferation seen at high magnification.

Immunohistochemistry (IHC) for collagen-I. The IHC staining was processed according to the standard IHC protocol at KCI Biotech. Anti-collagen-I antibody (Abcam; catalog [cat.] no. ab34710) was used. The stained slides were then scanned with a Hamamatsu NanoZoomer digital pathology S210 slide scanner and analyzed using the software to calculate the positive staining area/analysis area (%) or positive staining cells per unit area.

Statistical analyses. Statistical analysis was performed using GraphPad Prism 6.0 software. Descriptive results were expressed as the mean \pm standard error of the mean (SEM) or mean \pm SD. Statistical comparisons were performed using *t* test, one-way analysis of variance test, or two-way analysis of variance test. $P < 0.05$ was considered statistically significant.

Data availability. All data are available in the main text or the supplemental materials. The compound ALD-R491 is available under a materials transfer agreement.

SUPPLEMENTAL MATERIAL

Supplemental material is available online only.

FIG S1, PDF file, 0.2 MB.

FIG S2, PDF file, 0.2 MB.

FIG S3, PDF file, 0.2 MB.

FIG S4, PDF file, 0.2 MB.

FIG S5, PDF file, 0.2 MB.

FIG S6, PDF file, 1.1 MB.

ACKNOWLEDGMENTS

This work was partially supported by grants from the Ministry of Science and Technology of China (2018YFA0801100 to Y.X.), from the Priority Academic Program Development of the Jiangsu Higher Education Institutes (PAPD) and the National Center for International Research (2017B01012 to Y.X.) and from Luoda Biosciences, Inc. (LD20150701 to J.W.). Aluda Pharmaceuticals, Inc., has utilized the nonclinical and preclinical services program offered by the National Institute of Allergy and Infectious Diseases, NIH, USA.

R.C. conceived the studies; Y.X. and R.C. designed the studies; Y.X. and R.C. supervised, and Z. Li, J.W., J. Zhou, L.M., B.Y., Z.Q., F.Z., Y.D., K.H., Z. Liu, and T.W. performed the *in vitro* studies. Z. Li, J.W., J. Zhou, and B.Y. contributed equally to this work. Z. Li, B.Y., and Y.D. performed transfection and pseudoviral infection experiments. J.W. and L.M. performed exosome experiments and pilot Treg experiments. Z. Li and K.H. performed macrophage experiments. Z. Li and K.H. performed *Salmonella* killing assays in R. Huang's lab at Soochow University. F.Z. performed immunofluorescence experiments. Z.Q. performed the FRAP experiments. Z. Liu performed cell preparation from animals for *in vitro* studies. J. Zhang supervised and J. Zhou performed Treg cell experiments. E.S. supervised and J.C. performed the lung fibrosis *in vivo* studies. J.G. supervised and W.W. performed *in vivo* drug tissue distribution studies. D.S. managed the SARS-CoV-2 *in vivo* project that was performed in R. Baric's lab at the University of

North Carolina. R.C. wrote the manuscript. All authors read, edited, and approved the final version of the manuscript.

Patents and pending patents on ALD-R491, its related compounds, and their uses are held by Aluda Pharmaceuticals, Inc., and Luoda Biosciences, Inc. R.C. is an employee of Aluda Pharmaceuticals, Inc. and a shareholder and the appointed legal representative of Luoda Biosciences, Inc.; L.M. and D.S. hold shares of Aluda Pharmaceuticals, Inc. All other authors declare no competing financial interests.

REFERENCES

1. Lavine JS, Bjornstad ON, Antia R. 2021. Immunological characteristics govern the transition of COVID-19 to endemicity. *Science* 371:741–745. <https://doi.org/10.1126/science.abe6522>.
2. Russell MW, Moldoveanu Z, Ogra PL, Mestecky J. 2020. Mucosal immunity in COVID-19: a neglected but critical aspect of SARS-CoV-2 infection. *Front Immunol* 11:611337. <https://doi.org/10.3389/fimmu.2020.611337>.
3. Froberg J, Diavatopoulos DA. 2021. Mucosal immunity to severe acute respiratory syndrome coronavirus 2 infection. *Curr Opin Infect Dis* 34: 181–186. <https://doi.org/10.1097/QCO.00000000000000724>.
4. Turner JS, O'Halloran JA, Kalaidina E, Kim W, Schmitz AJ, Zhou JQ, Lei T, Thapa M, Chen RE, Case JB, Amanat F, Rauseo AM, Haile A, Xie X, Klebert MK, Suessen T, Middleton WD, Shi PY, Krammer F, Teeffey SA, Diamond MS, Presti RM, Ellebedy AH. 2021. SARS-CoV-2 mRNA vaccines induce persistent human germinal centre responses. *Nature* 596:109–113. <https://doi.org/10.1038/s41586-021-03738-2>.
5. Reynolds CJ, Pade C, Gibbons JM, Butler DK, Otter AD, Menacho K, Fontana M, Smit A, Sackville-West JE, Cutino-Moguel T, Maini MK, Chain B, Noursadeghi M, Brooks T, Semper A, Manisty C, Treibel TA, Moon JC, Investigators UKC, Valdes AM, McKnight A, Altmann DM, Boyton R, UK COVIDsortium Immune Correlates Network. 2021. Prior SARS-CoV-2 infection rescues B and T cell responses to variants after first vaccine dose. *Science* 372:1418–1423. <https://doi.org/10.1126/science.abh1282>.
6. Hoffmann M, Hofmann-Winkler H, Kruger N, Kempf A, Nehlmeier I, Graichen L, Arora P, Sidarovitch A, Moldenhauer AS, Winkler MS, Schulz S, Jack HM, Stankov MV, Behrens GMN, Pohlmann S. 2021. SARS-CoV-2 variant B.1.617 is resistant to bamlanivimab and evades antibodies induced by infection and vaccination. *Cell Rep* 36:109415. <https://doi.org/10.1016/j.celrep.2021.109415>.
7. Planas D, Veyer D, Baidaliuk A, Staropoli I, Guivel-Benhassine F, Rajah MM, Planchais C, Porrot F, Robillard N, Puech J, Prot M, Gallais F, Gantner P, Vely A, Le Guen J, Kassis-Chikhani N, Edriss D, Belec L, Seve A, Courtellement L, Pere H, Hocqueloux L, Fafi-Kremer S, Prazuck T, Mouquet H, Bruel T, Simon-Loriere E, Rey FA, Schwartz O. 2021. Reduced sensitivity of SARS-CoV-2 variant Delta to antibody neutralization. *Nature* 596:276–280. <https://doi.org/10.1038/s41586-021-03777-9>.
8. He X, Lau EHY, Wu P, Deng X, Wang J, Hao X, Lau YC, Wong JY, Guan Y, Tan X, Mo X, Chen Y, Liao B, Chen W, Hu F, Zhang Q, Zhong M, Wu Y, Zhao L, Zhang F, Cowling BJ, Li F, Leung GM. 2020. Temporal dynamics in viral shedding and transmissibility of COVID-19. *Nat Med* 26:672–675. <https://doi.org/10.1038/s41591-020-0869-5>.
9. Wolfel R, Corman VM, Guggemos W, Seilmäier M, Zange S, Muller MA, Niemeyer D, Jones TC, Vollmar P, Rothe C, Hoelscher M, Bleicker T, Brunink S, Schneider J, Ehmann R, Zwirglmaier K, Drosten C, Wendtner C. 2020. Virological assessment of hospitalized patients with COVID-2019. *Nature* 581:465–469. <https://doi.org/10.1038/s41586-020-2196-x>.
10. Goldman JD, Lye DCB, Hui DS, Marks KM, Bruno R, Montejano R, Spinner CD, Galli M, Ahn MY, Nahass RG, Chen YS, SenGupta D, Hyland RH, Osinusi AO, Cao H, Blair C, Wei X, Gaggar A, Brainard DM, Towner WJ, Munoz J, Mullan KM, Marty FM, Tashima KT, Diaz G, Subramanian A, GS-US-540-5773 Investigators. 2020. Remdesivir for 5 or 10 days in patients with severe Covid-19. *N Engl J Med* 383:1827–1837. <https://doi.org/10.1056/NEJMoa2015301>.
11. Bouhaddou M, Memon D, Meyer B, White KM, Rezelj VV, Correa Marrero M, Polacco BJ, Melnyk JE, Ulferts S, Kaake RM, Batra J, Richards AL, Stevenson E, Gordon DE, Rojc A, Obernier K, Fabius JM, Soucheray M, Miorin L, Moreno E, Koh C, Tran QD, Hardy A, Robinot R, Vallet T, Nilsson-Payant BE, Hernandez-Armenta C, Dunham A, Weigang S, Knerr J, Modak M, Quintero D, Zhou Y, Dugourd A, Valdeolivas A, Patil T, Li Q, Huttenhain R, Cakir M, Muralidharan M, Kim M, Jang G, Tutuncuoglu B, Hiatt J, Guo JZ, Xu J, Bouhaddou S, Mathy CJP, Gaulton A, Manners EJ, et al. 2020. The global phosphorylation landscape of SARS-CoV-2 infection. *Cell* 182: 685–712.e19. <https://doi.org/10.1016/j.cell.2020.06.034>.
12. Gordon DE, Hiatt J, Bouhaddou M, Rezelj VV, Ulferts S, Braberg H, Jureka AS, Obernier K, Guo JZ, Batra J, Kaake RM, Weckstein AR, Owens TW, Gupta M, Pourmal S, Titus EW, Cakir M, Soucheray M, McGregor M, Cakir Z, Jang G, O'Meara MJ, Tummino TA, Zhang Z, Foussard H, Rojc A, Zhou Y, Kuchenov D, Huttenhain R, Xu J, Eckhardt M, Swaney DL, Fabius JM, Ummadi M, Tutuncuoglu B, Rathore U, Modak M, Haas P, Haas KM, Naing ZZC, Pulido EH, Shi Y, Barrio-Hernandez I, Memon D, Petsalaki E, Dunham A, Marrero MC, Burke D, Koh C, Vallet T, Zoonomia Consortium, et al. 2020. Comparative host-coronavirus protein interaction networks reveal pan-viral disease mechanisms. *Science* 370:eabe9403. <https://doi.org/10.1126/science.abe9403>.
13. Gordon DE, Jang GM, Bouhaddou M, Xu J, Obernier K, White KM, O'Meara MJ, Rezelj VV, Guo JZ, Swaney DL, Tummino TA, Huttenhain R, Kaake RM, Richards AL, Tutuncuoglu B, Foussard H, Batra J, Haas K, Modak M, Kim M, Haas P, Polacco BJ, Braberg H, Fabius JM, Eckhardt M, Soucheray M, Bennett MJ, Cakir M, McGregor MJ, Li Q, Meyer B, Roesch F, Vallet T, Mac Kain A, Miorin L, Moreno E, Naing ZZC, Zhou Y, Peng S, Shi Y, Zhang Z, Shen W, Kirby IT, Melnyk JE, Chorba JS, Lou K, Dai SA, Barrio-Hernandez I, Memon D, Hernandez-Armenta C, et al. 2020. A SARS-CoV-2 protein interaction map reveals targets for drug repurposing. *Nature* 583:459–468. <https://doi.org/10.1038/s41586-020-2286-9>.
14. Riva L, Yuan S, Yin X, Martin-Sancho L, Matsunaga N, Pache L, Burgstaller-Muehlbacher S, De Jesus PD, Teriete P, Hull MV, Chang MW, Chan JF, Cao J, Poon VK, Herbert KM, Cheng K, Nguyen TH, Rubanov A, Pu Y, Nguyen C, Choi A, Rathnasinghe R, Schotsaert M, Miorin L, Dejosez M, Zwaka TP, Sit KY, Martinez-Sobrido L, Liu WC, White KM, Chapman ME, Lendy EK, Glynne RJ, Albrecht R, Ruppin E, Mesecar AD, Johnson JR, Benner C, Sun R, Schultz PG, Su AI, Garcia-Sastre A, Chatterjee AK, Yuen KY, Chanda SK. 2020. Discovery of SARS-CoV-2 antiviral drugs through large-scale compound repurposing. *Nature* 586:113–119. <https://doi.org/10.1038/s41586-020-2577-1>.
15. Wang R, Simoneau CR, Kulsupatrakul J, Bouhaddou M, Travisano KA, Hayashi JM, Carlson-Steurermer J, Zengel JR, Richards CM, Fozouni P, Oki J, Rodriguez L, Joehnk B, Walcott K, Holden K, Sil A, Carette JE, Krogan NJ, Ott M, Puschnik AS. 2021. Genetic screens identify host factors for SARS-CoV-2 and common cold coronaviruses. *Cell* 184:106–119.e14. <https://doi.org/10.1016/j.cell.2020.12.004>.
16. Pan H, Peto R, Henao-Restrepo A-M, Preziosi M-P, Sathyamoorthy V, Abdool Karim Q, Alejandria MM, Hernández García C, Kiely M-P, Malekzadeh R, Murthy S, Reddy KS, Roses Perigo M, Abi Hanna P, Ader F, Al-Bader AM, Alhasawi A, Allum E, Alotaibi A, Alvarez-Moreno CA, Appadoo S, Asiri A, Aukrust P, Barratt-Due A, Bellani S, Branca M, Cappel-Porter HBC, Cerrato N, Chow TS, Como N, Eustace J, García PJ, Godbole S, Gotuzzo E, Griskevicius L, Hamra R, Hassan M, Hassany M, Hutton D, Irmansyah I, Jancorine L, Kirwan J, Kumar S, Lennon P, Lopardo G, Lydon P, Magrini N, Maguire T, Manevska S, Manuel O, WHO Solidarity Trial Consortium, et al. 2021. Repurposed anti-viral drugs for Covid-19 - interim WHO solidarity trial results. *N Engl J Med* 384:497–511. <https://doi.org/10.1056/NEJMoa2023184>.
17. Danielsson F, Peterson MK, Caldeira Araujo H, Lautenschlager F, Gad AKB. 2018. Vimentin diversity in health and disease. *Cells* 7:147. <https://doi.org/10.3390/cells7100147>.
18. Li Z, Paulin D, Lacolley P, Coletti D, Agbulut O. 2020. Vimentin as a target for the treatment of COVID-19. *BMJ Open Respir Res* 7:e000623. <https://doi.org/10.1136/bmjresp-2020-000623>.
19. Ramos I, Stamatakis K, Oeste CL, Perez-Sala D. 2020. Vimentin as a multi-faceted player and potential therapeutic target in viral infections. *Int J Mol Sci* 21:4675. <https://doi.org/10.3390/ijms21134675>.

20. Zhang Y, Wen Z, Shi X, Liu YJ, Eriksson JE, Jiu Y. 2020. The diverse roles and dynamic rearrangement of vimentin during viral infection. *J Cell Sci* 134:jcs250597. <https://doi.org/10.1242/jcs.250597>.
21. McDonald-Hyman C, Muller JT, Loschi M, Thangavelu G, Saha A, Kumari S, Reichenbach DK, Smith MJ, Zhang G, Koehn BH, Lin J, Mitchell JS, Fife BT, Panoskaltsis-Mortari A, Feser CJ, Kirchmeier AK, Osborn MJ, Hippen KL, Kelekar A, Serody JS, Turka LA, Munn DH, Chi H, Neubert TA, Dustin ML, Blazar BR. 2018. The vimentin intermediate filament network restrains regulatory T cell suppression of graft-versus-host disease. *J Clin Invest* 128:4604–4621. <https://doi.org/10.1172/JCI95713>.
22. dos Santos G, Rogel MR, Baker MA, Troken JR, Urich D, Morales-Nebreda L, Sennello JA, Kutuzov MA, Sitikov A, Davis JM, Lam AP, Cheresh P, Kamp D, Shumaker DK, Budinger GR, Ridge KM. 2015. Vimentin regulates activation of the NLRP3 inflammasome. *Nat Commun* 6:6574. <https://doi.org/10.1038/ncomms7574>.
23. Colucci-Guyon E, Portier MM, Dunia I, Paulin D, Pournin S, Babinet C. 1994. Mice lacking vimentin develop and reproduce without an obvious phenotype. *Cell* 79:679–694. [https://doi.org/10.1016/0092-8674\(94\)90533-3](https://doi.org/10.1016/0092-8674(94)90533-3).
24. Zhang L, Qu Z, Wu J, Yao S, Zhang Q, Zhang T, Mo L, Yao Q, Xu Y, Chen R. 2021. SARs of a novel series of s-triazine compounds targeting vimentin to induce methuotic phenotype. *Eur J Med Chem* 214:113188. <https://doi.org/10.1016/j.ejmech.2021.113188>.
25. Wu J, Xie Q, Liu Y, Gao Y, Qu Z, Mo L, Xu Y, Chen R, Shi L. 2021. A small vimentin-binding molecule blocks cancer exosome release and reduces cancer cell mobility. *Front Pharmacol* 12:627394. <https://doi.org/10.3389/fphar.2021.627394>.
26. Kalluri R, LeBleu VS. 2020. The biology, function, and biomedical applications of exosomes. *Science* 367:eaa6977. <https://doi.org/10.1126/science.aau6977>.
27. Ghosh S, Dellibovi-Ragheb TA, Kerviel A, Pak E, Qiu Q, Fisher M, Takvorian PM, Bleck C, Hsu VW, Fehr AR, Perlman S, Achar SR, Straus MR, Whittaker GR, de Haan CAM, Kehrl J, Altan-Bonnet G, Altan-Bonnet N. 2020. Beta-coronaviruses use lysosomes for egress instead of the biosynthetic secretory pathway. *Cell* 183:1520–1535.e14. <https://doi.org/10.1016/j.cell.2020.10.039>.
28. Boumaza A, Gay L, Mezouar S, Bestion E, Diallo AB, Michel M, Desnues B, Raoult D, La Scola B, Halfon P, Vitte J, Olive D, Mege JL. 2021. Monocytes and macrophages, targets of severe acute respiratory syndrome coronavirus 2: the clue for coronavirus disease 2019 immunoparalysis. *J Infect Dis* 224:395–406. <https://doi.org/10.1093/infdis/jiab044>.
29. Grant RA, Morales-Nebreda L, Markov NS, Swaminathan S, Querrey M, Guzman ER, Abbott DA, Donnelly HK, Donayre A, Goldberg IA, Klug ZM, Borkowski N, Lu Z, Kihshen H, Politanska Y, Sichizya L, Kang M, Shilatifard A, Qi C, Lomasney JW, Argento AC, Kruser JM, Malsin ES, Pickens CO, Smith SB, Walter JM, Pawlowski AE, Schneider D, Nannapaneni P, Abdala-Valencia H, Bharat A, Gottardi CJ, Budinger GRS, Misharin AV, Singer BD, Wunderink RG, NU SCRIPT Study Investigators. 2021. Circuits between infected macrophages and T cells in SARS-CoV-2 pneumonia. *Nature* 590:635–641. <https://doi.org/10.1038/s41586-020-03148-w>.
30. Mor-Vaknin N, Legembre M, Yu Y, Serezani CH, Garg SK, Jatzek A, Swanson MD, Gonzalez-Hernandez MJ, Teitz-Tennenbaum S, Punturieri A, Engleberg NC, Banerjee R, Peters-Golden M, Kao JY, Markovitz DM. 2013. Murine colitis is mediated by vimentin. *Sci Rep* 3:1045. <https://doi.org/10.1038/srep01045>.
31. Qin C, Zhou L, Hu Z, Zhang S, Yang S, Tao Y, Xie C, Ma K, Shang K, Wang W, Tian DS. 2020. Dysregulation of immune response in patients with coronavirus 2019 (COVID-19) in Wuhan, China. *Clin Infect Dis* 71:762–768. <https://doi.org/10.1093/cid/ciaa248>.
32. Sadeghi A, Tahmasebi S, Mahmood A, Kuznetsova M, Valizadeh H, Taghizadieh A, Nazemiyeh M, Aghebati-Maleki L, Jadidi-Niaragh F, Abbaspour-Aghdam S, Roshangar L, Mikaeili H, Ahmadi M. 2021. Th17 and Treg cells function in SARS-CoV2 patients compared with healthy controls. *J Cell Physiol* 236:2829–2839. <https://doi.org/10.1002/jcp.30047>.
33. Wang Y, Zheng J, Islam MS, Yang Y, Hu Y, Chen X. 2021. The role of CD4 (+)FoxP3(+) regulatory T cells in the immunopathogenesis of COVID-19: implications for treatment. *Int J Biol Sci* 17:1507–1520. <https://doi.org/10.7150/ijbs.59534>.
34. Rahimzadeh M, Naderi N. 2021. Toward an understanding of regulatory T cells in COVID-19: a systematic review. *J Med Virol* 93:4167–4181. <https://doi.org/10.1002/jmv.26891>.
35. Stephen-Victor E, Das M, Karnam A, Pitard B, Gautier JF, Bayry J. 2020. Potential of regulatory T-cell-based therapies in the management of severe COVID-19. *Eur Respir J* 56:2002182. <https://doi.org/10.1183/13993003.02182-2020>.
36. Dinnon KH 3rd, Leist SR, Schafer A, Edwards CE, Martinez DR, Montgomery SA, West A, Yount BL Jr, Hou YJ, Adams LE, Gully KL, Brown AJ, Huang E, Bryant MD, Choong IC, Glenn JS, Gralinski LE, Sheahan TP, Baric RS. 2020. A mouse-adapted model of SARS-CoV-2 to test COVID-19 countermeasures. *Nature* 586:560–566. <https://doi.org/10.1038/s41586-020-2708-8>.
37. Wu C, Chen X, Cai Y, Xia J, Zhou X, Xu S, Huang H, Zhang L, Zhou X, Du C, Zhang Y, Song J, Wang S, Chao Y, Yang Z, Xu J, Zhou X, Chen D, Xiong W, Xu L, Zhou F, Jiang J, Bai C, Zheng J, Song Y. 2020. Risk factors associated with acute respiratory distress syndrome and death in patients with coronavirus disease 2019 pneumonia in Wuhan, China. *JAMA Intern Med* 180:934–943. <https://doi.org/10.1001/jamainternmed.2020.0994>.
38. George PM, Wells AU, Jenkins RG. 2020. Pulmonary fibrosis and COVID-19: the potential role for antibiotic therapy. *Lancet Respir Med* 8:807–815. [https://doi.org/10.1016/S2213-2600\(20\)30225-3](https://doi.org/10.1016/S2213-2600(20)30225-3).
39. Li FJ, Surolia R, Li H, Wang Z, Liu G, Kulkarni T, Massicano AVF, Mobley JA, Mondal S, de Andrade JA, Coonrod SA, Thompson PR, Wille K, Lapi SE, Athar M, Thannickal VJ, Carter AB, Antony VB. 2021. Citrullinated vimentin mediates development and progression of lung fibrosis. *Sci Transl Med* 13:ea2927. <https://doi.org/10.1126/scitranslmed.aba2927>.
40. Challa AA, Stefanovic B. 2011. A novel role of vimentin filaments: binding and stabilization of collagen mRNAs. *Mol Cell Biol* 31:3773–3789. <https://doi.org/10.1128/MCB.05263-11>.
41. Surolia R, Li FJ, Wang Z, Li H, Dsouza K, Thomas V, Mirov S, Perez-Sala D, Athar M, Thannickal VJ, Antony VB. 2019. Vimentin intermediate filament assembly regulates fibroblast invasion in fibrogenic lung injury. *JCI Insight* 4:e123253. <https://doi.org/10.1172/jci.insight.123253>.
42. Singh TU, Parida S, Lingaraju MC, Kesavan M, Kumar D, Singh RK. 2020. Drug repurposing approach to fight COVID-19. *Pharmacol Rep* 72:1479–1508. <https://doi.org/10.1007/s43440-020-00155-6>.
43. Delorey TM, Ziegler CGK, Heimberg G, Normand R, Yang Y, Segerstolpe Å, Abbondanza D, Fleming SJ, Subramanian A, Montoro DT, Jagadeesh KA, Dey KK, Sen P, Slyper M, Pita-Juárez YH, Phillips D, Biermann J, Bloom-Ackermann Z, Barkas N, Ganna A, Gomez J, Melms JC, Katsyv I, Normandin E, Naderi P, Popov YV, Raju SS, Niezen S, Tsai LT-Y, Siddle KJ, Sud M, Tran VM, Vellarikkal SK, Wang Y, Amir-Zilberstein L, Atri DS, Beechem J, Brook OR, Chen J, Divakar P, Dorceus P, Engreitz JM, Essene A, Fitzgerald DM, Fropf R, Gazal S, Gould J, Grzyb J, Harvey T, Hecht J, et al. 2021. COVID-19 tissue atlases reveal SARS-CoV-2 pathology and cellular targets. *Nature* 595:107–113. <https://doi.org/10.1038/s41586-021-03570-8>.
44. Rendeiro AF, Ravichandran H, Bram Y, Chandar V, Kim J, Meydan C, Park J, Foox J, Hether T, Warren S, Kim Y, Reeves J, Salvatore S, Mason CE, Swanson EC, Borczuk AC, Elemento O, Schwartz RE. 2021. The spatial landscape of lung pathology during COVID-19 progression. *Nature* 593:564–569. <https://doi.org/10.1038/s41586-021-03475-6>.
45. Hookway C, Ding L, Davidson MW, Rappoport JZ, Danuser G, Gelfand VI. 2015. Microtubule-dependent transport and dynamics of vimentin intermediate filaments. *Mol Biol Cell* 26:1675–1686. <https://doi.org/10.1091/mbc.E14-09-1398>.
46. Styers ML, Kowalczyk AP, Faundez V. 2005. Intermediate filaments and vesicular membrane traffic: the odd couple's first dance? *Traffic* 6:359–365. <https://doi.org/10.1111/j.1600-0854.2005.00286.x>.
47. Yu YT, Chien SC, Chen LY, Lai CT, Tsay YG, Chang SC, Chang MF. 2016. Surface vimentin is critical for the cell entry of SARS-CoV. *J Biomed Sci* 23:14. <https://doi.org/10.1186/s12929-016-0234-7>.
48. Suprawicz L, Swoger M, Gupta S, Pikel E, Byfield FJ, Iwamoto DV, Germann DA, Reszec J, Marcinczyk N, Jamney P, Schwarz JM, Bucki R, Patteson A. 2021. Vimentin binds to SARS-CoV-2 spike protein and antibodies targeting extracellular vimentin block in vitro uptake of SARS-CoV-2 virus-like particles. *bioRxiv* <https://doi.org/10.1101/2021.01.08.425793>.
49. Zhou P, Yang XL, Wang XG, Hu B, Zhang L, Zhang W, Si HR, Zhu Y, Li B, Huang CL, Chen HD, Chen J, Luo Y, Guo H, Jiang RD, Liu MQ, Chen Y, Shen XR, Wang X, Zheng XS, Zhao K, Chen QJ, Deng F, Liu LL, Yan B, Zhan FX, Wang YY, Xiao GF, Shi ZL. 2020. A pneumonia outbreak associated with a new coronavirus of probable bat origin. *Nature* 579:270–273. <https://doi.org/10.1038/s41586-020-1212-7>.
50. Patterson BK, Francisco EB, Yogendra R, Emily Long E, Pise A, Rodrigues H, Hall E, Herrera M, Parikh P, Guevara-Coto J, Triche T, Scott P, Hekmati S, Maglione D, Chang X, Rodriguez R, Mora J. 2021. Persistence of SARS-CoV-2 S1 protein in CD16+ monocytes in post-acute sequelae of COVID-19 (PASC) up to 15 months post-infection. *bioRxiv* <https://doi.org/10.1101/2021.06.25.449905>.
51. Abassi Z, Knaney Y, Karram T, Heyman SN. 2020. The lung macrophage in SARS-CoV-2 infection: a friend or a foe? *Front Immunol* 11:1312. <https://doi.org/10.3389/fimmu.2020.01312>.

52. Nikitina E, Larionova I, Choinzonov E, Kzhyshkowska J. 2018. Monocytes and macrophages as viral targets and reservoirs. *Int J Mol Sci* 19:2821. <https://doi.org/10.3390/ijms19092821>.
53. Park MD. 2020. Macrophages: a Trojan horse in COVID-19? *Nat Rev Immunol* 20:351. <https://doi.org/10.1038/s41577-020-0317-2>.
54. Marshall M. 2020. The lasting misery of coronavirus long-haulers. *Nature* 585:339–341. <https://doi.org/10.1038/d41586-020-02598-6>.
55. Prigge A, Ma R, Coates B, Ridge KM. 2020. Deletion of vimentin in regulatory T cells augments suppression without altering homeostasis. *Am J Respir Crit Care Med* 201:A5565–A5565. https://doi.org/10.1164/ajrccm-conference.2020.201.1_MeetingAbstracts.A5565.
56. Arpaia N, Green JA, Moltedo B, Arvey A, Hemmers S, Yuan S, Treuting PM, Rudensky AY. 2015. A distinct function of regulatory T cells in tissue protection. *Cell* 162:1078–1089. <https://doi.org/10.1016/j.cell.2015.08.021>.
57. Fabbri L, Moss S, Khan F, Chi W, Xia J, Robinson K, Smyth A, Jenkins G, Stewart I. 2021. Post-viral parenchymal lung disease of COVID-19 and viral pneumonitis: a systematic review and meta-analysis. *medRxiv* <https://doi.org/10.1101/2021.03.15.21253593>.
58. Matute-Bello G, Downey G, Moore BB, Groshong SD, Matthay MA, Slutsky AS, Kuebler WM, Acute Lung Injury in Animals Study Group. 2011. An official American Thoracic Society workshop report: features and measurements of experimental acute lung injury in animals. *Am J Respir Cell Mol Biol* 44:725–738. <https://doi.org/10.1165/rccb.2009-0210ST>.
59. Schmidt ME, Knudson CJ, Hartwig SM, Pewe LL, Meyerholz DK, Langlois RA, Harty JT, Varga SM. 2018. Memory CD8 T cells mediate severe immunopathology following respiratory syncytial virus infection. *PLoS Pathog* 14:e1006810. <https://doi.org/10.1371/journal.ppat.1006810.g001>.